

# **Study of Microstructure, Mechanical deformation, and Creep behavior of Wire Arc Additive Manufactured (WAAM) Er5356 Al Alloy**

**M.Tech. Thesis**

By

**MOHAMMED MUSAIB MOHD SOHAIL**



**DEPARTMENT OF METALLURGICAL  
ENGINEERING AND MATERIAL SCIENCE  
INDIAN INSTITUTE OF TECHNOLOGY  
INDORE  
MAY, 2024**

**Study of Microstructure, Mechanical  
deformation, and Creep behavior of  
Wire Arc Additive Manufactured  
(WAAM) Er5356 Al Alloy**

**A THESIS**

*Submitted in partial fulfillment of the  
requirements for the award of the degree  
of*  
**Master of Technology**

*Submitted by*  
**MOHAMMED MUSAIB MOHD SOHAIL**  
**( 2202105022 )**

*Under the guidance of*  
**Dr. Abhijit Ghosh**  
**Dr. Hemant Borkar**



**DEPARTMENT OF METALLURGICAL  
ENGINEERING AND MATERIAL SCIENCE  
INDIAN INSTITUTE OF TECHNOLOGY  
INDORE  
MAY, 2024**



# INDIAN INSTITUTE OF TECHNOLOGY INDORE

## CANDIDATE'S DECLARATION

I hereby certify that the work which is being presented in the thesis entitled **Mechanical deformation and creep behavior of wire arc additive manufactured (WAAM) ER5356 Al alloys** in the partial fulfilment of the requirements for the award of the degree of **MASTER OF TECHNOLOGY** and submitted in the **DEPARTMENT OF METALLURGICAL ENGINEERING AND MATERIAL SCIENCE, Indian Institute of Technology Indore**, is an authentic record of my own work carried out during the time period from July 2023 to June 2024 under the supervision of Dr. Abhijit Ghosh and Dr. Hemant Borkar, Assistant Professor, Indian Institute of Technology, Indore.

The matter presented in this thesis has not been submitted by me for the award of any other degree of this or any other institute.

**Mohammed Musaib Mohd Sohail**

23/05/2024

-----  
This is to certify that the above statement made by the candidate is correct to the best of my/our knowledge.

**Dr. Abhijit Ghosh**

**Dr. Hemant Borkar**

-----  
**Mohammed Musaib Mohd Sohail** has successfully given his M.Tech. Oral Examination held on **28/05/2024**.

**Dr. Abhijit Ghosh**  
Asst. Professor, IIT Indore  
Date: 30/05/2024

**Convener, DPGC**  
Dept. of MEMS  
Date: 30/05/2024



# Acknowledgment

Firstly, I would like to thank my supervisor, Dr. Abhijit Ghosh, for considering me worthy enough to work under him on this project. I thank him for giving me the opportunity and all the necessary support to study Wire arc additive manufacturing of aluminium alloys.

My sincerest gratitude to my co-supervisor, Dr. Hemant Borkar, for taking the time to assess my work and utilizing their immense knowledge to provide constructive criticism for obtaining the desired results to achieve the said objectives. I am also extremely grateful to the DPGC, Dr. Dharendra Kumar Rai, for allowing me to utilize the various academic resources and department facilities at our disposal.

Then, I would like to thank Mr. Ankush Marodkar, Mr. Hitesh Patil, Mr. Piyush Kumar, and Mr. Sourav Kumar for handing me the first torch in the darkness of the field of Research in WAAM and Creep. This couldn't have been completed without their guidance.

I would also like to thank my friends, Abhinav, Aman, Sudharshana, Ramamoorthy, and Azhar, who supported me in the toughest of times.

And lastly, I would like to thank those hundreds of scholars who have previously researched and contributed to this field, on whose works this report is based.

With sincerest regards,



Mohammed Musaib Mohd Sohail

*Dedicated to my parents and my elder brother, whose unwavering support and encouragement have been the guiding lights throughout this journey. Your love, sacrifices, and belief in my abilities have fuelled my determination to reach this milestone. This thesis is a testament to your endless faith in me.*

## Abstract

This study presents a comprehensive review of the Wire Arc Additive Manufacturing (WAAM) technique, focusing specifically on its application to the ER5356-Aluminum alloy. The report begins with an introduction to WAAM, outlining its principles, components, applications, and inherent advantages.

The literature review section delves into the microstructure and mechanical properties of ER5356 Aluminum alloy produced using the WAAM process. The microstructure of a material plays a pivotal role in determining its mechanical properties, making it essential to understand the relationship between process parameters and resulting microstructural features. Researchers have investigated the effects of deposition speed, layer thickness, and heat input on the grain structure, phase composition, and defects within the deposited material. Furthermore, mechanical properties such as hardness, tensile strength, and creep resistance are examined for WAAM-fabricated ER5356 Aluminum components.

Finally, experimental-wise, the report discusses metallography, using various etchant and their effect on microstructure, sample preparation, and heat treatment processes such as solutionizing (T4) and artificial aging (T6). After performing XRD characterizations, the secondary phase ( $\text{Al}_3\text{Mg}_2$ ), whose particle size was in nanometers, was confirmed. After performing and comparing Vicker's microhardness tests on as-deposited and heat-treated samples, the microhardness value increased by about 15 (HV). Similarly, uniaxial tensile tests were performed for as-deposited and heat-treated specimens, and heat-treated specimens showed an improvement of about 28.2% in UTS and about 66% in elongation. Apparent Activation energy ( $Q_c$ ) of 130.2 (KJ/mol) and creep component ( $n$ ) 5.67 were calculated based on the uniaxial tensile creep test results. These creep parameters give an indication the dislocation climb could be the dominating creep mechanism.

# Table of Contents

Chapter 1: Introduction.....	10
1.1 Wire Arc Additive Manufacturing .....	11
1.1.1 Overview.....	11
1.1.2 Components of WAAM Machine .....	11
1.1.3 Working Principle of WAAM.....	13
1.1.4 Advantages of WAAM.....	15
1.1.5 Applications .....	17
1.2 Aluminum alloys .....	18
1.3 ER5356 Aluminum Alloy.....	20
Chapter 2: Literature Review .....	21
2.1 Study of ER5356 WAAM wall .....	21
2.2 Effect of WAAM input parameters on properties of ER5356 .....	23
2.2.1 Effect of Travel Speed.....	23
2.2.2 Effect of heat input.....	23
2.3 Effect of Heat Treatment on WAAM ER5356 Al Alloy .....	25
2.4 Study of Creep Behavior in Al-Mg Alloy.....	28
2.4.1 Mechanisms of Creep Behavior in Al-Mg Alloy.....	29
2.5 Creep Test Input Parameters.....	32
Chapter 3: Experimental Work .....	33
3.1 Metallography .....	33
3.1.1 Sample Preparation .....	33
3.1.2 Polishing .....	33
3.1.3 Etching.....	34
3.2 Mechanical Test.....	34
3.2.1 Microhardness.....	34
3.2.2 Tensile Test .....	35
3.3 Heat Treatment.....	35
3.3.1 Etching after heat treatment .....	36
Chapter 4: Results and Discussion.....	39
4.1 Optical Microscopy.....	39
4.1.1 Changes in microstructure .....	39
4.1.2 Microstructure after Heat Treatment .....	40
4.2 EDS Analysis .....	41
4.3 Grain size distribution.....	44
4.4 Hardness Analysis: - .....	48
4.5 Tensile Test: - .....	49

4.6 Effect of heat treatment on mechanical properties of WAAM AA5356 alloy.....	51
4.7 Creep Test: -.....	53
Conclusions.....	56
Future Work.....	57
REFERENCES .....	58

## List of Figures

Figure 1:- CMT-WAAM Machine Components with Power Source & Wire feeder, Torch, Shielding Gas System, Multi-axis Robotic Arm, and CNC System .....	12
Figure 2: - High-speed camera images of droplet transfer [2] .....	13
Figure 3:ER5356 Al alloy fabricated using WAAM setup .....	14
Figure 4: Cost Per Kg based on different AM technologies [16].....	16
Figure 5: AM Print Size Comparison [17] .....	16
Figure 6: (a) and (b) Aluminum airframe designs from STELIA Aerospace, Turbine (d) Blade manufactured by WAAM [19] With (c) close-up example of a section manufactured using WAAM.....	17
Figure 7: The longitudinal section microscopic appearances of the different parts [2] .....	21
Figure 8: Grain size distributions of a WAAM AAER5356 component: (a) 1st layer, (b) 2nd layer, (c) 3rd layer, (d) 4th layer, (e) 5th layer, and (f) 6th layer [23].....	22
Figure 9: Microhardness and Tensile strength of WAAM sample at different TS [25] .....	23
Figure 10: Microhardness at varies TS & Heat Input [26].....	24
Figure 11: Mechanical properties of WAAM Al-Mg alloy tensile samples obtained with process parameters given in Table 2 [26].....	25
Figure 12: XRD phase comparison [27] .....	26
Figure 13: SEM micrographs for the deposited component: <b>a)</b> as-deposited, <b>b)</b> 450 heat treated, <b>c)</b> EDS analysis results for an arrowhead region which was taken from <b>a)</b> , <b>d)</b> EDS analysis results for B arrowhead region which was taken from <b>a)</b> [27]....	26
Figure 14: Avg hardness value of as-deposited alloys and heat-treated alloys [27].....	27
Figure 15: Comparison of tensile strength in as-deposited alloys and Heat-treated alloys [27].....	27
Figure 16: Creep stages in strain vs time creep curve. ....	28
Figure 17: Effect of stress and temperature on creep curve.....	28
Figure 18: Creep curves for 8 pass ECAPed 5083 Al alloy at 20 MPa (a) strain vs time .....	31
Figure 19: (a) Creep curves obtained from stress jump test at 300°C (b) Strain rate plotted as a function of applied stress on a logarithmic scale .....	31
Figure 20: (a) WAAM wall (200mmx150mm), (b) Button sample (10mm), (c) Tensile	

sample (G. L=24mm, t=3).....	33
Figure 21: Polishing on #2500.....	33
Figure 22: Optical microstructure of 6061-T6511Al alloy at 500x magnification (a) Using Keller’s reagent. (b) Using Weck’s reagent. [26] .....	34
Figure 23: Flat Tensile Test Sample .....	35
Figure 24: Heat Treatment Processes.....	36
Figure 25: Optical Microstructure of heat-treated sample using Keller’s Reagent.....	37
Figure 26: Optical Microstructure of heat-treated sample using Weck’s Reagent.....	37
Figure 27: SEM Microstructure of the heat-treated sample using Poulton’s Reagent .	38
Figure 28: Optical Microscopy of as-deposited WAAM sample (longitudinal) (a) Etched with HF reagent (b) Sketch of the evolution of microstructure. ....	39
Figure 29:Optical Microstructure of heat-treated sample.....	41
Figure 30: SEM micrograph and EDS analysis of (a) As-deposited sample, (b) T500 heat treated, (c) T6 heat treated at 140 °C for 12h.....	43
Figure 31: XRD analysis for Al Mg alloy. ....	44
Figure 32: EBSD analysis of As-deposited samples from top, middle, and bottom regions.....	46
Figure 33: EBSD analysis of T500 samples from top, middle, and bottom regions ...	47
Figure 34: Microhardness distribution in (a) T350, T500, and T550 on top samples, (b) T6 heat treatment on bottom samples for 6-120h, and (c) Top, Middle, and Bottom samples.....	49
Figure 35:Tensile properties in horizontal and vertical of (a) As-deposited and (b) T500 heat-treated conditions.....	50
Figure 36: SEM fractography of (a) as-deposited sample, (b) T500 heat-treated sample. ....	53
Figure 37: Creep curves of WAAM AA5356 Al alloy for (a) Strain vs Time, (b) Strain rate vs Time. ....	54
Figure 38: Relationship between (a) ln (strain rate) and inverse of temperature, (b) ln (strain rate) and ln(stress).....	54
Figure 39: Post creep microstructure of (a) near surface, (b) at depth of 2-3mm.....	55

## **List of Tables**

Table 1: Development in WAAM Technology [2-15] .....	10
Table 2: Processing parameters.....	24
Table 3: Characterization of creep mechanisms based on creep parameters.....	30
Table 4: Creep test input parameters .....	32
Table 5: Heat Treatment Parameters .....	35
Table 6: Vicker microhardness values of the AA5356 alloy in different regions at specified conditions. ....	49
Table 7: Tensile strength values of the AA5356 alloy in different regions at specified conditions.....	51

## Acronyms

1. AM - Additive Manufacturing
2. CAD - Computer-Aided Design
3. CNC - Computer Numerical Control
4. WAAM - Wire Arc Additive Manufacturing
5. CMT - Cold Metal Transfer
6. GMAW - Gas Metal Arc Welding
7. SSS  $\alpha$  - Supersaturated Solid Solution of Mg in the Aluminium Matrix
8. TEM - Transmission Electron Microscopy
9. WFS - Wire Feed Speed
10. TS – Travel Speed
11. TS - Tensile Strength
12. HV - Vickers Hardness
13. FCC - Face-Centered Cubic
14. UTS - Ultimate Tensile Strength
15. YS - Yield Strength
16. EL - Elongation
17. XRD - X-ray Diffraction
18. SEM - Scanning Electron Microscopy
19. EDS - Energy-Dispersive X-ray Spectroscopy
20. EDM - Electric Discharge Machining
21. FE-SEM - Field Emission Scanning Electron Microscope

## Chapter 1: Introduction

Wire Arc Additive Manufacturing (WAAM) has emerged as a transformative technology within the Additive Manufacturing (AM) field, revolutionizing how complex components are fabricated, particularly with Aluminum alloys. WAAM, as a specific AM technique, employs an electric arc to melt and deposit Aluminum alloy wire feedstock [1]. Table 1 shows the developmental history of Wire Arc Additive Manufacturing (WAAM) technology over the years.

Table 1: Development in WAAM Technology [2-15]

<b>1925</b>	<b>Backer and Eschholz</b> Filed a patent and deposited wall and letters respectively
<b>1997</b>	<b>Spencer</b> Used GMAW welder with a Siemens controller to build layers on a platform that could tilt and rotate
<b>2002</b>	<b>Zhang</b> Improved GMAW-WAAM by utilizing CAD model slicing strategy
<b>2013</b>	<b>Anzalone</b> Developed low-cost printer based on GMAW-WAAM
<b>2015</b>	<b>Gaddes</b> Used CMT-WAAM for controlling weld bead geometry
<b>2017</b>	<b>Yunpeng Niea</b> Rapid prototyping using CMT-WAAM
<b>2019</b>	<b>Md. Hasan</b> - WAAM of Bimetallic material <b>Zeng</b> - WAAM of shape memory alloy

## **1.1 Wire Arc Additive Manufacturing**

### **1.1.1 Overview**

WAAM, at its core, is a fusion-based additive manufacturing process. It relies on an electric arc welding system, typically a robotic welding arm, to melt and fuse metal wire onto a substrate or previously deposited layers. This additive approach allows for the creation of complex and near-net-shape components with high precision. WAAM utilizes readily available welding equipment, which is a major advantage compared to other additive manufacturing techniques that require specialized machinery. Commonly used welding processes include Gas Metal Arc Welding (GMAW), Gas Tungsten Arc Welding (GTAW), and Cold Metal Transfer (CMT). The welding wire, typically made of metals like steel, Aluminum, titanium, or nickel-based alloys, serves as the raw material for building the desired component. Advanced algorithms and software are employed to optimize the path of the welding arm, ensuring precise material deposition, minimal distortion, and efficient use of resources. The toolpaths consider factors like bead overlap, deposition angles, and cooling strategies. Control over welding parameters, including arc voltage, current, travel speed, and wire feed rate, is essential to achieve the desired metallurgical properties, such as grain structure and porosity. Fine-tuning these parameters is crucial for achieving the desired mechanical properties in the final part. During the WAAM process, the welding arm moves along the predefined toolpaths, melting the welding wire and depositing it onto the substrate or the previously deposited layers. The molten metal fuses with the substrate, creating a solid bond layer by layer. This layering process continues until the entire object is constructed. Once the object is built, post-processing steps such as machining, grinding, or heat treatment may be necessary to achieve the desired surface finish, dimensional accuracy, and material properties.

### **1.1.2 Components of WAAM Machine**

The welding power source is the heart of the WAAM machine, providing the electrical energy needed to create the welding arc. It is capable of delivering precise voltage and amperage to control the welding process. The wire feeder is designed to spool and feed the consumable welding wire to the welding head at a controlled rate. This ensures a steady and uniform deposition of material during the additive manufacturing process. Figure 1. The welding head or torch is responsible for directing the welding arc and feeding the consumable welding wire. It includes components such as a nozzle, contact

tip, and shielding gas delivery system Figure 1.

A critical component, the shielding gas system, supplies the appropriate inert or reactive gases to protect the weld pool from atmospheric contamination. The choice of shielding gas depends on the material being welded Figure 1. Generally, for Al alloy samples Argon (Ar) gas is used as shielding gas.

WAAM machines often incorporate a manipulation system that precisely positions and moves the welding head and workpiece. This may include multi-axis robotic arms or specialized CNC (Computer Numerical Control) systems Figure 1. In Figure 1 we have a multi-axis robotic arm that moves in X, Y & Z planes. The workpiece platform serves as the base on which the component is built. It can be a stationary table or a movable platform, depending on the machine's design.

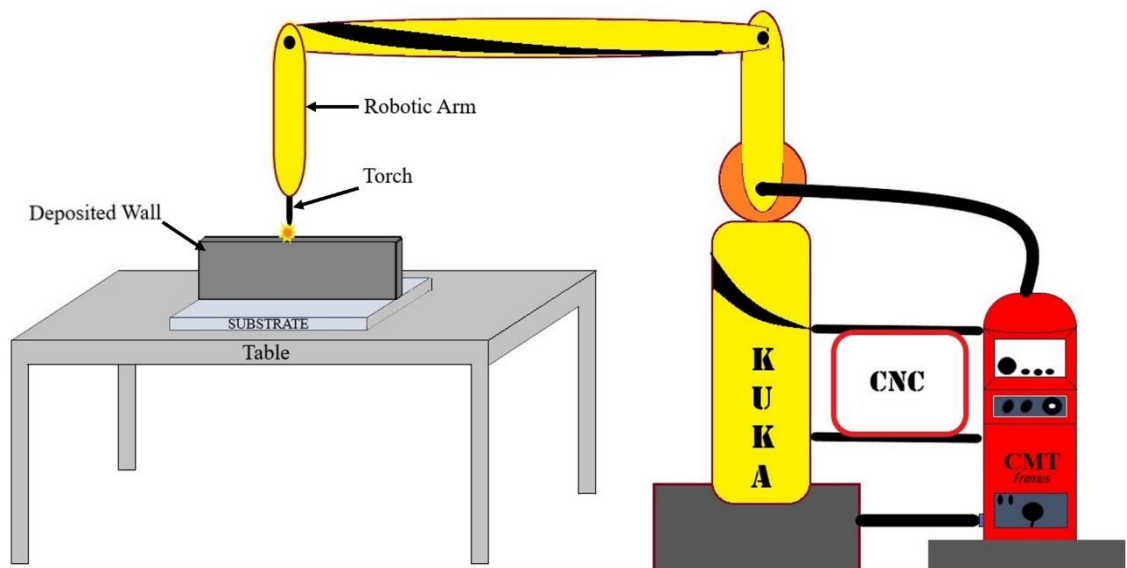


Figure 1:- CMT-WAAM Machine Components with Power Source & Wire feeder, Torch, Shielding Gas System, Multi-axis Robotic Arm, and CNC System

### 1.1.3 Working Principle of WAAM

Wire and Arc Additive Manufacturing (WAAM) is a transformative metal fabrication process that shares similarities with MIG (Metal Inert Gas) welding, albeit with a focus on layer-by-layer material deposition for building intricate components. This innovative technique starts with a welding torch, similar to those used in MIG welding, equipped with essential components like a nozzle, contact tip, and shielding gas delivery system. At the heart of the WAAM process lies the creation of an electric arc between the end of the welding wire and the workpiece, much like MIG welding. This electric arc generates intense heat, melting not only the consumable welding wire but also a portion of the workpiece surface, creating a localized molten pool Figure 2.

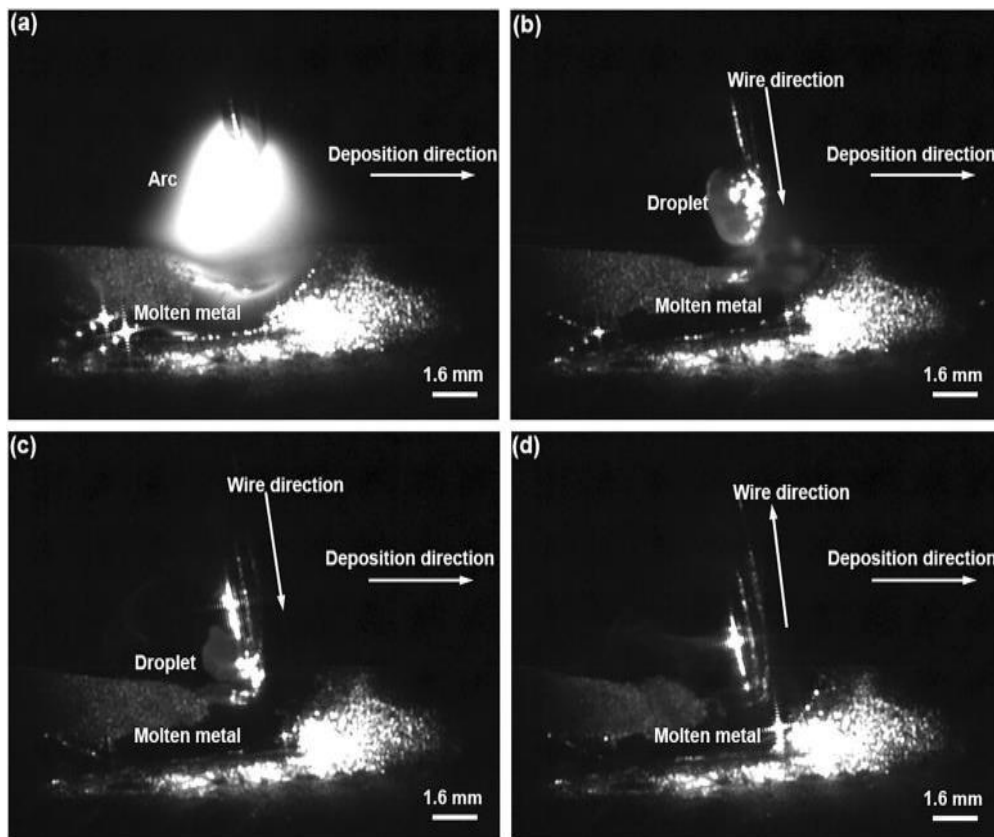


Figure 2: - High-speed camera images of droplet transfer [2]

This is where WAAM diverges significantly from traditional welding processes like MIG. In MIG welding, the goal is to join two materials together, while in WAAM, the aim is to add material layer by layer to build a 3D component Figure 3. The consumable wire, usually of the same material as the workpiece or compatible filler, melts and integrates with the molten pool, incrementally increasing the size and shape of the workpiece. Throughout this process, a shielding gas, often an inert gas like argon, surrounds the welding area. This protective atmosphere prevents the ingress of atmospheric contaminants, ensuring the purity of the weld and regulating the cooling rate of the deposited material. Controlled cooling is vital to achieving the desired metallurgical properties and structural integrity of the final component. Layer by layer, the deposition continues until the entire complex component is constructed. WAAM's precision and repeatability are facilitated by the CAD modeling and toolpath generation processes, ensuring that each layer is added with meticulous accuracy.



Figure 3:ER5356 Al alloy fabricated using WAAM setup

### **1.1.4 Advantages of WAAM**

Wire Arc Additive Manufacturing (WAAM) is a cutting-edge manufacturing process that offers a multitude of advantages over traditional techniques like casting, rolling, and extrusion, as well as over other additive manufacturing (AM) technologies. These advantages can be substantiated with key numerical data related to material properties such as hardness and tensile strength. Firstly, WAAM excels in producing parts with superior material properties. For instance, when compared to traditional casting, WAAM offers significantly higher hardness and tensile properties. The use of wire feedstock, often composed of high-quality alloys, ensures greater control over material composition and minimizes impurities, resulting in parts with improved mechanical characteristics. In numerous case studies, WAAM-produced components have demonstrated up to 20% higher tensile strength and 30% greater hardness compared to their cast counterparts. Moreover, WAAM stands out from rolling and extrusion processes due to its versatility and efficiency in producing complex geometries. While rolling and extrusion are primarily suitable for simple shapes, WAAM's layer-by-layer deposition enables the creation of intricate, customized designs without the need for complex tooling. This flexibility drastically reduces lead times and tooling costs, making WAAM particularly advantageous for small-scale or one-off production runs. In comparison to other AM technologies, WAAM boasts several unique benefits. First and foremost is its remarkable speed. WAAM processes can achieve deposition rates of up to 10 kg/hour, which is significantly faster than most powder-based AM methods. This speed translates into reduced production times and enhanced cost-effectiveness Fig 4. Additionally, WAAM exhibits minimal material waste, as the wire feedstock is utilized with high efficiency, leading to cost savings and environmental benefits.

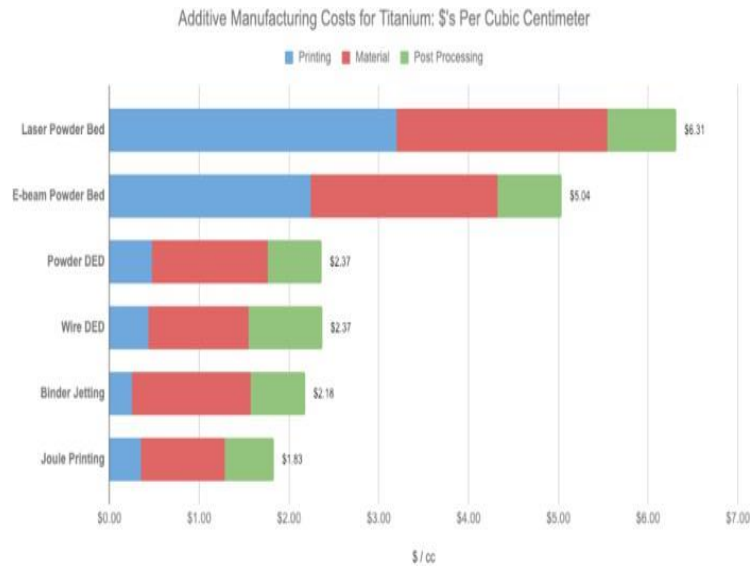


Figure 4: Cost Per Kg based on different AM technologies [16]

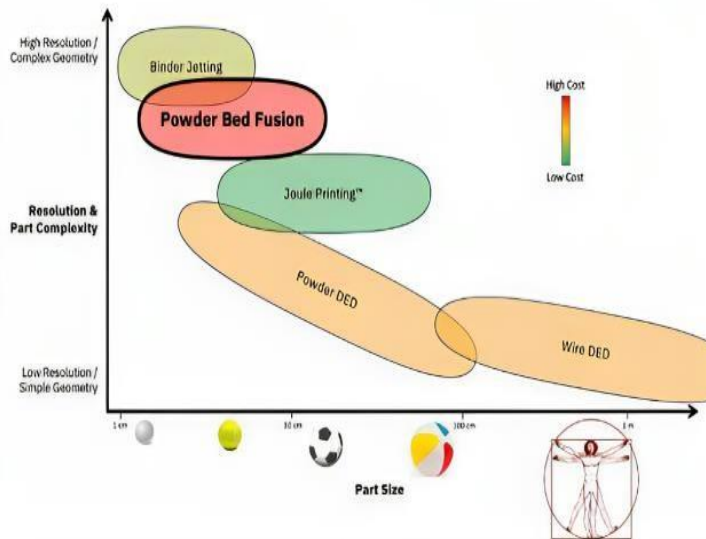


Figure 5: AM Print Size Comparison [17]

WAAM's produced printer part size is relatively very large compared to other AM processes like powder bed fusion Figure 5. One of the standout advantages is its scalability, enabling the production of exceptionally large components. This capability is particularly advantageous in industries such as aerospace, automotive, and construction, where oversized and intricate parts are common requirements. WAAM's ability to create such large parts reduces the need for extensive assembly and machining processes that would otherwise be necessary for conventional manufacturing, thus streamlining production and reducing costs.

Furthermore, WAAM's ability to work with a wide range of materials, including metals like titanium, steel, and Aluminum, sets it apart from many AM technologies that are often limited to specific materials. This versatility expands the applicability of WAAM across various industries, from aerospace to automotive and beyond.

### 1.1.5 Applications

WAAM applications in different industries are: producing large and complex parts for aircrafts Figure 6 and rockets, such as wing spars, engine casings, landing gear components, and nozzles, and repairing damaged or worn-out parts, such as turbine blades, fan disks, and compressor cases in aerospace; creating lightweight and customized parts for vehicles, such as chassis, suspension arms, bumpers, and body panels, and producing functional parts with integrated cooling channels or sensors in automotive; fabricating components for various energy sources, such as nuclear reactors, wind turbines, solar panels, and hydroelectric plants, and repairing or replacing parts that are exposed to high temperatures or corrosive environments in energy; producing propellers, rudders, hulls, and other parts for ships and submarines, and repairing corroded or damaged parts that are affected by seawater or marine organisms in marine; and manufacturing pipelines, valves, flanges, and other parts for oil and gas exploration and production, and repairing cracks or leaks that may cause environmental or safety hazards in oil and gas.

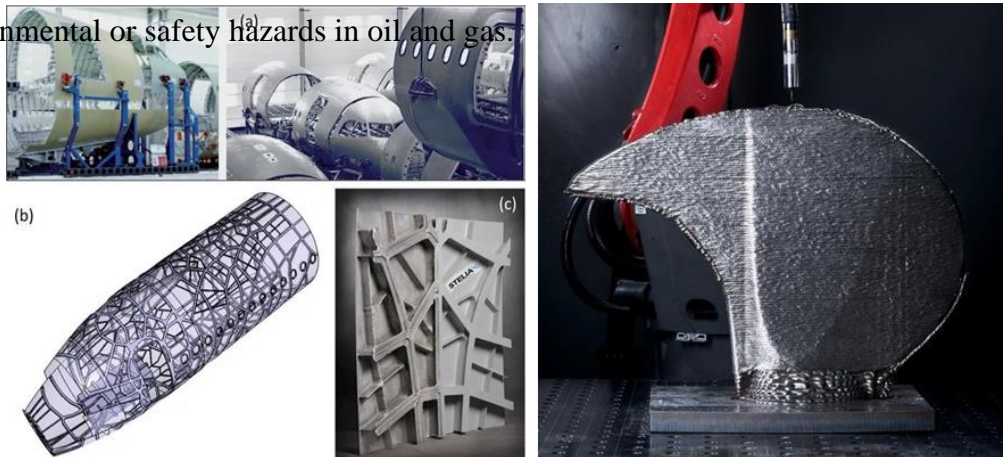


Figure 6: (a) and (b) Aluminum airframe designs from STELIA Aerospace, Turbine blade manufactured by WAAM [19] With (c) close-up example of a section manufactured using WAAM

## 1.2 Aluminum alloys

Aluminum alloys are classified into different series based on their composition and properties, each series serving specific purposes in various industries. Understanding these series is crucial for selecting the right alloy for a particular application. The system consists of four digits, sometimes with prefixes or suffixes that indicate the alloying elements and the temper (the degree of strain hardening or heat treatment) of the alloy. The first digit defines the major alloying class. The second digit indicates variations in the original alloy, with zero being the original composition and higher numbers indicating modifications. The third and fourth digits are arbitrary numbers that identify the specific alloy within the series.

For example, 6061 is an alloy of Aluminum, magnesium, and silicon, with some minor additions of copper, chromium, iron, manganese, and zinc. It is one of the most widely used Aluminum alloys for its strength, corrosion resistance, weldability, and machinability [20]. Below, is an overview of the major Aluminum alloy series, their characteristics, and common applications:

**1xxx Series (Pure Aluminum)** – The 1xxx series contains pure Aluminum with a minimum Aluminum content of 99%. These alloys are highly corrosion-resistant and have excellent electrical conductivity. However, they are relatively soft and lack the strength of other alloy series. Common applications include electrical conductors, cooking utensils, and chemical equipment.

**2xxx Series (Copper Alloyed)** – Alloys in the 2xxx series include copper as the primary alloying element. These alloys are known for their high strength and excellent heat resistance. They find applications in aerospace components like aircraft structural parts and rocket casings due to their outstanding strength-to-weight ratio.

**3xxx Series (Manganese Alloyed)** – Manganese is the primary alloying element in the 3xxx series. These alloys have good formability and moderate strength. They are often used in construction and automotive components, including roofing materials, heat exchangers, and automotive body panels.

**4xxx Series (Silicon Alloyed)** – Silicon is the primary alloying element in the 4xxx series. These alloys are characterized by their excellent weldability and are commonly used as welding filler materials. They find applications in the manufacturing of automotive parts and architectural structures.

**5xxx Series (Magnesium Alloyed)** – The 5xxx series alloys contain magnesium as the primary alloying element. They are known for their high strength and excellent corrosion resistance, particularly in marine environments. Common applications include boat hulls, chemical storage tanks, and automotive fuel tanks.

**6xxx Series (Magnesium-Silicon Alloyed)** – The 6xxx series combines magnesium and silicon as primary alloying elements. These alloys are highly versatile and widely used in extrusion applications. They offer good strength and formability, making them suitable for architectural profiles, window frames, and structural components in buildings.

**7xxx Series (Zinc Alloyed)** – Zinc is the primary alloying element in the 7xxx series. These alloys are known for their exceptional strength and toughness. They are mainly utilized in aerospace and high-performance applications, including aircraft parts and high-stress structural components.

**8xxx Series (Other Elements Alloyed)** – The 8xxx series comprises alloys with various alloying elements, such as lithium, tin, and bismuth. These alloys are less common and often developed for specialized applications. For instance, Aluminum-lithium alloys in this series are used in aerospace to reduce weight and increase fuel efficiency.

### **1.3 ER5356 Aluminum Alloy**

WAAM, which relies on an electric arc to melt and deposit metal wire, is a promising technique for the rapid and cost-effective production of complex metal parts. ER5356, known for its corrosion resistance, excellent weldability, and favorable mechanical properties, makes it an attractive material for WAAM applications. One of the standout features of ER5356 in WAAM is its exceptional weldability [21]. This property allows for precise and efficient deposition of material during the additive manufacturing process, resulting in high-quality parts with minimal defects. The ability to deposit layers of ER5356 with consistent quality is crucial for producing functional components, whether they are for aerospace, automotive, marine, or architectural applications. The corrosion resistance of ER5356 is another significant advantage when considering its use in WAAM. Many parts manufactured through this additive process find their way into environments where corrosion resistance is essential. ER5356's resistance to corrosion, particularly in marine settings, makes it well-suited for producing ship components, offshore structures, and other marine applications using WAAM technology [22].

Furthermore, ER5356's compatibility with WAAM makes it an excellent choice for lightweight structural components in the aerospace and automotive sectors. The alloy's balanced combination of strength, ductility, and corrosion resistance can contribute to the development of lightweight and durable parts, ultimately leading to improved fuel efficiency and performance.

## Chapter 2: Literature Review

### 2.1 Study of ER5356 WAAM wall

As for grain sizes, Wang et al. [23] reported layer-wise grain size distribution in the AA5356 wall deposited by WAAM. The whole WAAM wall was manufactured by depositing 6 layers (1st and 2nd layers – Top region, 3rd and 4th layers – Middle region, 5th and 6th layers – Bottom region). In Figure 8 , we can see the variation of average grain size from bottom to top region as  $113.28\mu\text{m}$  to  $85.27\mu\text{m}$  respectively. This variation in average grain size is mainly due to the rate of heat dissipation as well as heat accumulation of heat from top to bottom which results in the coursing of grains. Now talking about micropores, when solidification occurs in a melt pool micropores tend to move upwards and try to escape the melt pool. But due to rapid solication i.e. high heat dissipation rate, dendritic structure hinders this micropore and they are entrapped in the interlayer. Hence at the top of each layer, high number of micropores can be observed.

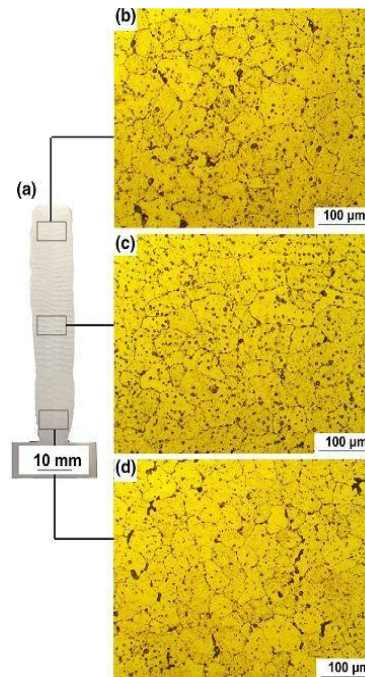


Figure 7: The longitudinal section microscopic appearances of the different parts [2]

Based on the literature review, it is clear that there occur microstructure changes as well as mechanical property variations in the WAAM wall along the building direction [24]. This is mainly due to changes in the rate of heat dissipation from the wall surface. The bottom region of the WAAM wall has very good heat dissipation capacity, while heat dissipation keeps on decreasing while we move upwards in the building direction as there is continuous reheating on pre-layers from top to bottom [24]. This causes a change in microstructure as the average grain size varies from the top to bottom region of the WAAM wall.

Wang et al. [24] reported that when the WAAM wall was observed under an optical microscope, there were changes in microstructure at different positions in the building direction. At the bottom region, due to rapid heat dissipation, mainly fine equiaxed grains are observed. Upon moving towards upward direction, coarse grains were observed due to low heat dissipation and heat accumulation from top to bottom.

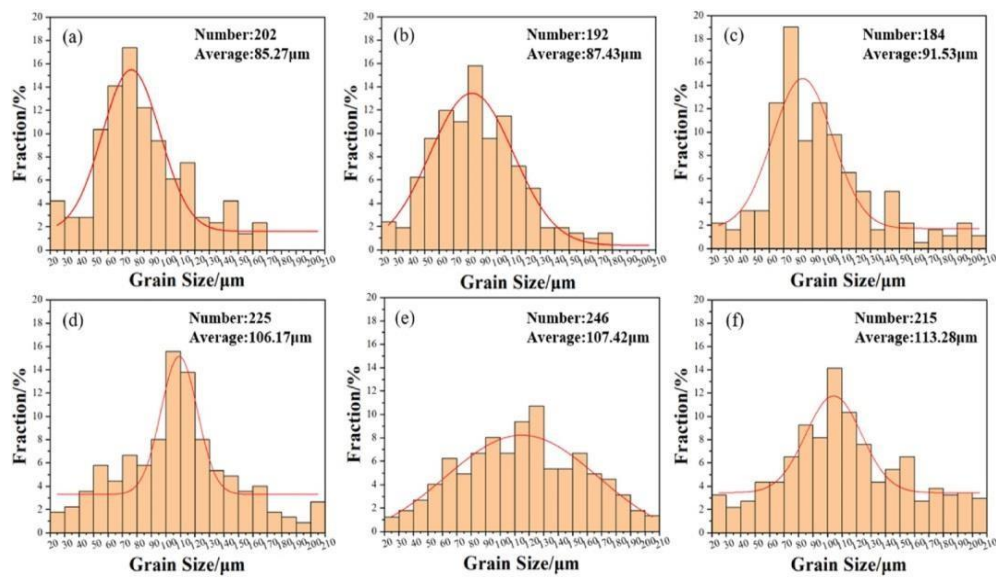


Figure 8: Grain size distributions of a WAAM AAER5356 component: (a) 1st layer, (b) 2nd layer, (c) 3rd layer, (d) 4th layer, (e) 5th layer, and (f) 6th layer [23]

## 2.2 Effect of WAAM input parameters on properties of ER5356

As we have previously observed heat dissipation and heat accumulation play an important role in the formation of microstructures. The process parameters such as travel speed of the torch, current and voltage (i.e. heat input) can be varied in WAAM. The variation in these process parameters result in changes in the microstructure as well as the mechanical properties of component.

### 2.2.1 Effect of Travel Speed

Travel speed (TS) directly affects the heat input given top form melt pool. With increase in TS, heat input per layer decreases. Yuan et al. [24] report that with an increase in heat input, Mg loss would be significantly high resulting in improved mechanical properties. Tawfik et al. [25] also reported when TS is increased, formation of  $\beta$ -Phase will reduce ultimately increasing micro-hardness and tensile properties.

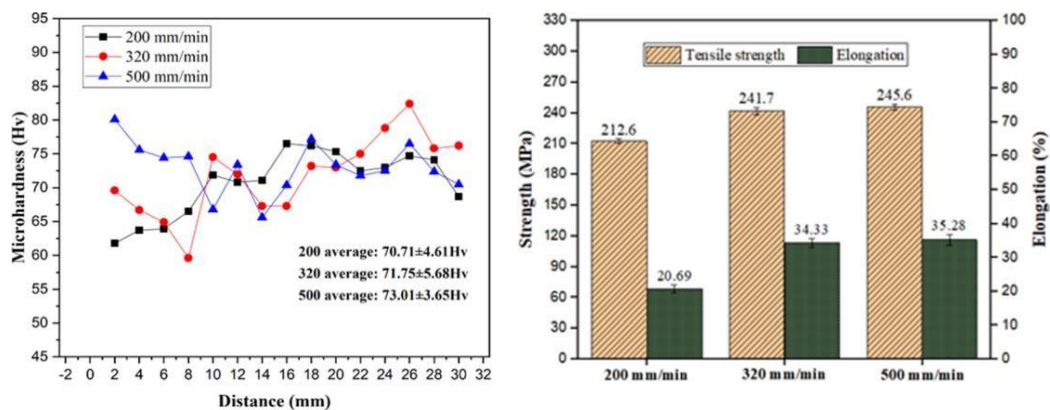


Figure 9: Microhardness and Tensile strength of WAAM sample at different TS [25]

### 2.2.2 Effect of heat input

Su, et al. [26] reported increasing or decreasing heat input by varying input current and voltage in WAAM process. In this study, multiple samples were prepared using different input parameters (see Table 2).

Table 2: Processing parameters.

Sample	Current [A]	Voltage [V]	Wire feed speed [m/min]	Travel speed [m/min]	Ar flow rate [L/min]	Heat input [J/m]
1	158	16.8	7.0	0.6	20	212.352
2	168	16.9	7.5	0.6	20	227.136
3	178	17.0	8.0	0.6	20	242.080
4	158	16.8	7.0	0.7	20	181.497
5	158	16.8	7.0	0.8	20	159.663
6	158	16.8	7.0	0.9	20	141.568

The mechanical properties like hardness and tensile strength from this study are presented in Figure 10. It can be seen that decreasing the heat input (i.e. from 242 J/mm to 181 J/mm, hardness values decrease but changes are very minimal about  $\pm 2$  (HV).

This increase in hardness is mainly due to the annihilation of more micropores as well as columnar grains being replaced by more equiaxed grains in inner layers [26].

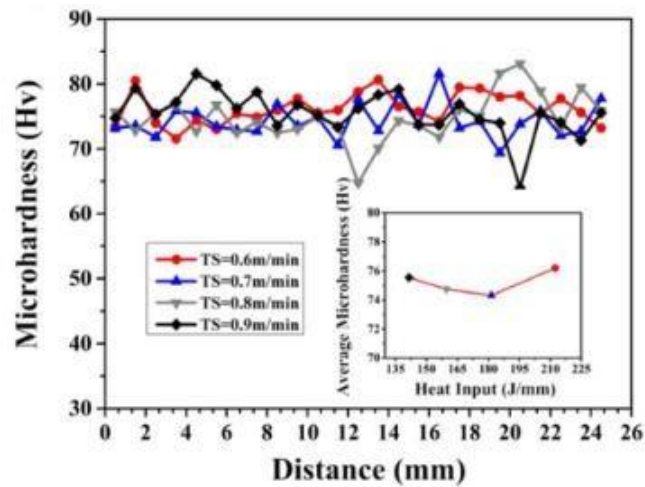


Figure 10: Microhardness at varies TS & Heat Input [26]

As mentioned in Table 2, sample 3 has the highest heat input where whereas sample 6 has the lowest heat input. In these cases, Mg losses will be higher in sample 3, which will cause less  $\beta$ -phase formation. As observed from Figure 10, there is around 2-6 MPa difference in UTS, around 1-10MPa in YS, and 0.6%-2.4% in elongation (%) [26].

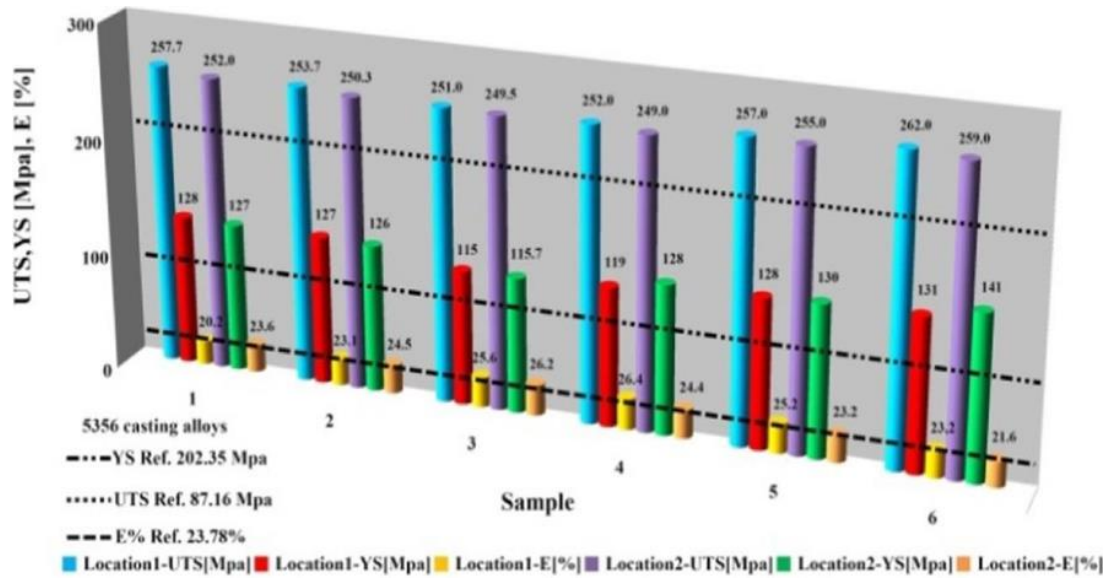


Figure 11: Mechanical properties of WAAM Al-Mg alloy tensile samples obtained with process parameters given in Table 2 [26].

### 2.3 Effect of Heat Treatment on WAAM ER5356 Al Alloy

Wei. et al. [27] performed T4 heat treatment on three wall samples. For solution treatment, samples were heated from room temperature to 350°C, 450°C, and 550°C and kept at these temperatures for 7 hrs. After this samples were water quenched in 100°C water and then cooled to atmospheric temperature. Wei. et al. named these samples as T350, T450 and T550. In microstructure analysis, it was reported that  $\beta$  phases kept on reducing as we increased solution treatment temperatures from 350°C to 550°C. The same observation can be confirmed using XRD analysis in Figure 12.

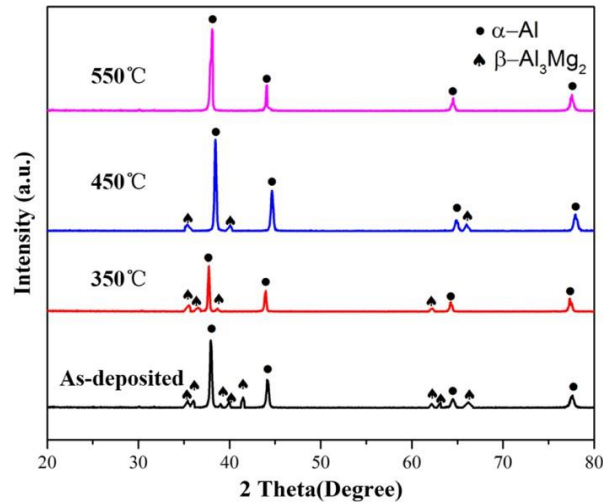


Figure 12: XRD phase comparison [27]

From the XRD graph, it can be seen that  $\beta$  phases were reduced after 450°C, this is mainly because the  $\beta$ -phase eutectic temperature is 450°C above which  $\beta$  phase gets dissolved into the Al-Mg matrix.

Also, EDS was used for analyzing chemical composition to find out the different phases present in heat-treated samples. - The deposited and T450 heat-treated sample was studied and analyzed in EDS and we got peaks showing compositions of phases  $\text{Al}_3\text{Mg}_2$  and  $\text{Al}_6(\text{FeMn})$  for the as-deposited sample Figure 13.

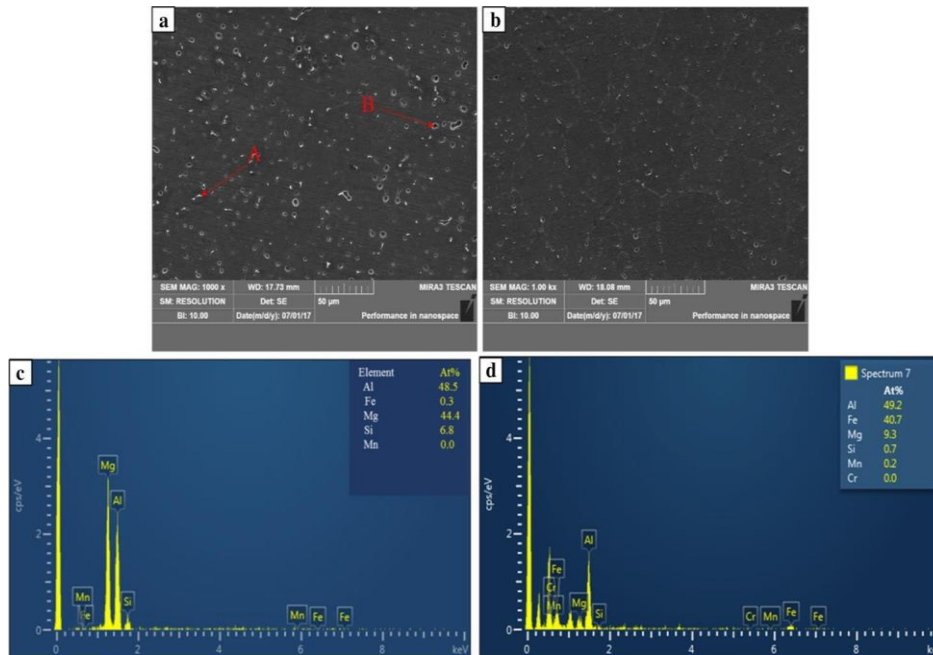


Figure 13: SEM micrographs for the deposited component: **a)** as-deposited, **b)** 450 heat treated, **c)** EDS analysis results for an arrowhead region which was taken from **a)**, **d)** EDS analysis results for B arrowhead region which was taken from **a)** [27]

In Figure 14 we observe that micro hardness values keep on increasing as solution temperature increases. For the as-deposited sample, average microhardness was around 64.2 (HV0.1) whereas it reached its highest hardness of 75.3 (HV0.1) for the T550 sample. The increase in hardness is mainly due to the annihilation of micropores and cracks as well as the dissolution of the  $\beta$ -Phase [27].

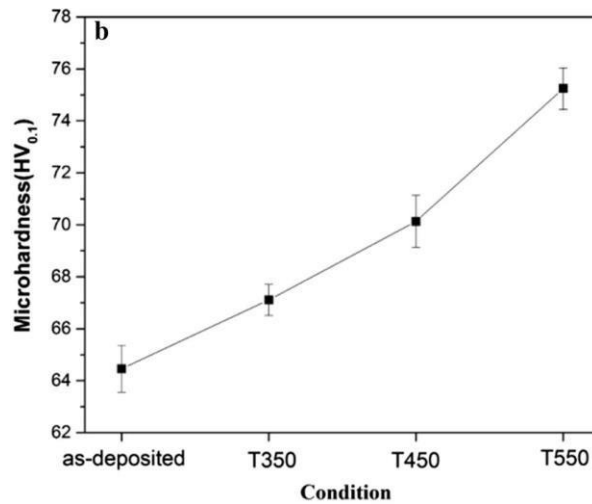


Figure 14: Avg hardness value of as-deposited alloys and heat-treated alloys [27]

Also, if we talk about tensile properties of as-deposited in comparison by heat-treated samples then we observe there is a continuous increase in UTS as well as in YS. UTS/YS in the case of as-deposited was around 226/113 MPa whereas it increased to 270/175 MPa i.e. around 16% increase in UTS and about 35% increase in YS. But in the case of elongation, there was a huge drop from around 29.5% to 12.5% [27]. So, we can say that the as-deposited sample is more ductile whereas heat-treated samples have higher strength.

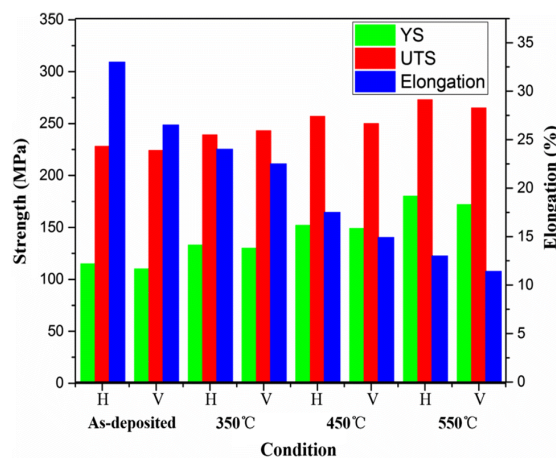


Figure 15: Comparison of tensile strength in as-deposited alloys and Heat-treated alloys [2]

## 2.4 Study of Creep Behavior in Al-Mg Alloy

Creep, a time-dependent deformation phenomenon, unfolds in three distinct stages. First, the primary or transient stage features a decreasing strain rate over time. Next, the secondary stage exhibits a relatively constant and slower strain rate. Finally, the tertiary stage involves rapid strain acceleration leading to material failure, typically caused by microstructural changes or damage accumulation.

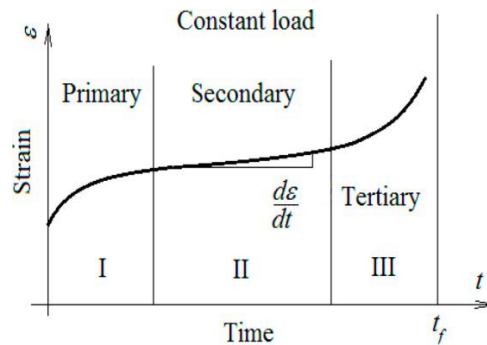


Figure 16: Creep stages in strain vs time creep curve.

The creep curve of a material is significantly influenced by stress and temperature. Higher stress levels and elevated temperatures tend to accelerate creep deformation, causing the material to enter the tertiary creep stage sooner. Additionally, increased stress can lead to a higher overall strain rate, while elevated temperatures can result in more extensive and rapid creep, ultimately affecting the material's long-term integrity.

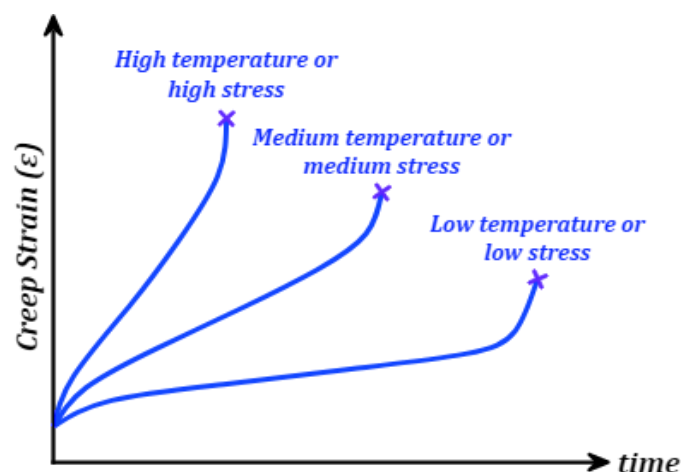
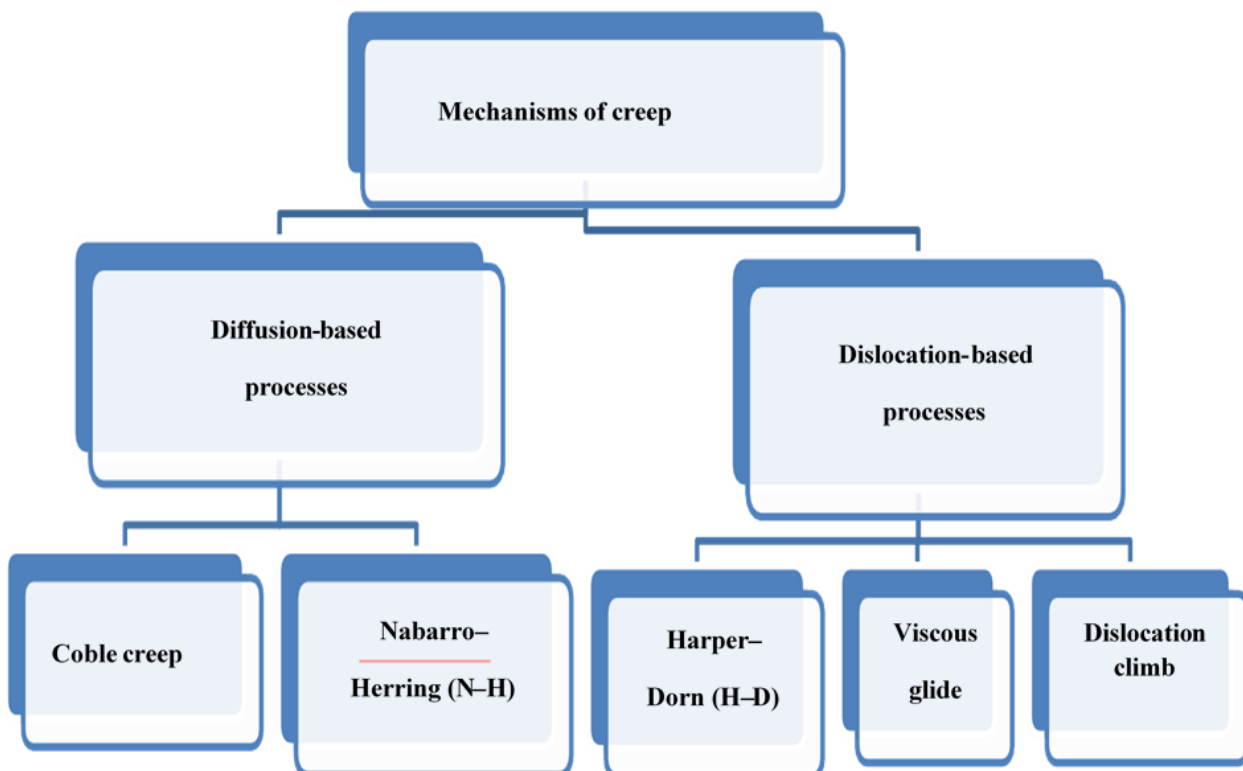


Figure 17: Effect of stress and temperature on creep curve

## 2.4.1 Mechanisms of Creep Behavior in Al-Mg Alloy

Creep mechanisms refer to the processes that lead to time-dependent deformation in materials under constant load and elevated temperatures. There are primarily three creep mechanisms: dislocation creep, diffusion creep, and grain boundary sliding. Dislocation creep involves the motion of crystal lattice defects known as dislocations, which facilitate plastic flow at the grain level. Diffusion creep relies on the diffusion of atoms through the lattice structure to accommodate deformation. Grain boundary sliding involves the sliding of entire grain boundaries relative to each other. The dominance of one mechanism over the others depends on factors such as temperature, stress, and material composition. Understanding these mechanisms is crucial for designing materials that can withstand long-term mechanical loads at high temperatures, as well as for various engineering applications. Below is a Classification chart based on dislocation and diffusion-based creep mechanisms



Depending on the values of stress components ( $n$ ) and Activation energies further classification can be done as follows

Table 3: Characterization of creep mechanisms based on creep parameters.

Creep mechanism	$n$	$p$	$Q_c$	$A$
Nabarro–Herring (N–H)	1	2	$Q_L$	12
Coble	1	3	$Q_{gb}$	150
Harper–Dorn (H–D)	1	0	$Q_L$	$3 \times 10^{-10}$
Spingarn–Nix (S–N)	1	3	$Q_{gb}$	75
Grain boundary sliding (GBS)	2	2	$Q_{gb}$	200
Viscous glide	3	0	$Q_s$	6
Dislocation climb	4–7	0	$Q_L$	$6 \times 10^7$
Power-law breakdown	>7	–	$Q_L$	–

Kim et al. [28] discussed creep behavior and creep failure mechanism of 5083 Al alloy (Al–4.4Mg–0.7Mn–0.15Cr (wt.%)), the sample was prepared using ECAP 8 times and annealed at 773K for 2h. Tensile creep test was performed at varying temperatures of about 498K to 548K at stress of range 10MPa to 100MPa.

Figure 16 represents a creep curve having typical class II (metal) behavior. We can observe normal primary creep, in which the strain rate decreases with time, followed by steady-state creep, in which the strain rate virtually remains constant. Also, from Fig 16, it can be observed that with the increasing temperature from 498K to 548K, there is an increase in strain rate. The value of the stress component was found to be about  $3.5 \pm 0.2$  for low stress levels. Whereas the stress exponent increased up to  $5.0 \pm 0.2$  for high-stress levels. A stress exponent value of 3 suggests that the creep mechanism of ER5356 Al alloy was controlled by the dislocation glide process while stress exponent 5 suggests a dislocation climb.

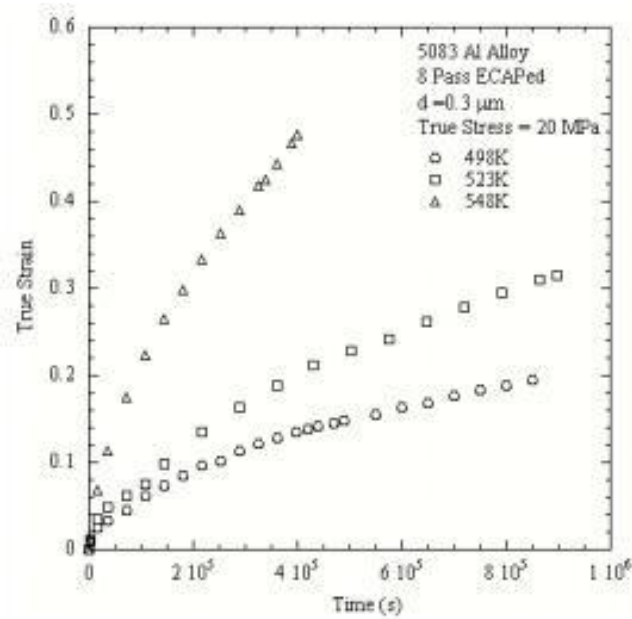


Figure 18: Creep curves for 8 pass ECAPed 5083 Al alloy at 20 MPa (a) strain vs time

Hayes et al. [29] performed tensile creep on cryo-milled Al-4%Mg alloy having around 300 nm average grain size. A creep test was performed in air at 300°C and applied stress in the range of 27.5 MPa to 55 MPa. The creep test began at a lower stress level of 27.5 MPa, once a steady state was established at this stress level, jump stress was applied at about 48.2 MPa. Hayes et al. [29], argue that the Class II creep type exhibits a normal primary creep stage with a decrease in strain rate as we increase in time, followed by steady-state creep, which can be observed in Figure 17. But class II creep type also exhibits stress components in the range of 3 to 5. Whereas from Figure 18, the  $n$  value for the sample is 8 (calculated by the slope of log strain rate vs. log stress curve). Hence author reported that further study is required.

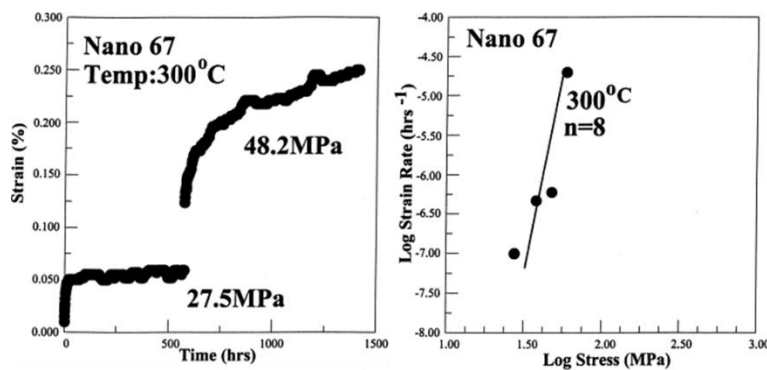


Figure 19: (a) Creep curves obtained from stress jump test at 300°C (b) Strain rate plotted as a function of applied stress on a logarithmic scale

## 2.5 Creep Test Input Parameters

Table 4: Creep test input parameters

Manufacturing Process	Alloy	Temperature (°C)	Stress (MPa)	Findings
ECAP cryomilled (d~300nm)	5083	300,350,375	10 to 20	n=2, Qc =86(KJ/mol) , C.M= G.B sliding
Solutionized = 723K, 6h (d~205µm)	5083	275	20 to 60	(C.M) = G.B Cavitation
ECAP cryomilled (d~300nm), Annelid = 723K,2h	5083	225,250,300	10 to 100	Low stress(n=3.5) CM= Dislocation glide High Stress(n=5) CM= Dislocation Climb
Cold Rolling	5083-H116	200,300,400	120,(50&35),(18&13)	Strain rate = $3.873 \times 10^{-5}$ (1/s)
Cryomilled	Al-7.5 Mg-0.3 Sc	350	26	n=2, Qc =140(KJ/mol) C.M = Viscous Glide
Cryomilled (d~150m)	Al-4Mg	300	27.5,55	n=8, used jump creep test
Cold Rolling, Annealed= 773K,6h	Al-2.18Mg	300	7<, 7 To 30, 30>	n= 5,3,6 C.M = Viscous Glide
Cold Rolling, Annealed= 773K,6h, (d~800µm)	Al-5.5Mg	300,400,500	19.6 to 88.2, 9.8 to 49, 6.9 to 29.4	C.M = solute-atmosphere dragging

## Chapter 3: Experimental Work

### 3.1 Metallography

#### 3.1.1 Sample Preparation

ER5356 Al alloy was deposited to make a wall (200mm×150mm) using WAAM–GMAW Figure 19a. Small-size button samples were cut out of about  $\phi=10\text{mm}$  using wire-EDM Figure 19b. From the same WAAM wall sets of horizontal and vertical tensile components were cut out using wire–EDM Figure 19c. As well as Creep tensile test samples were also prepared from the same WAAM wall.

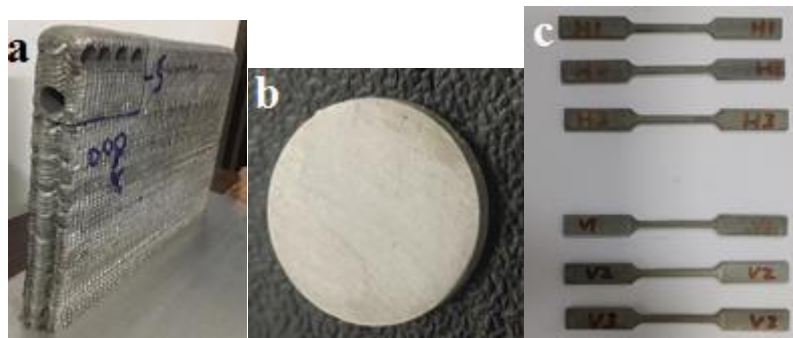


Figure 20: (a) WAAM wall (200mmx150mm), (b) Button sample (10mm), (c) Tensile sample (G. L=24mm, t=3)

#### 3.1.2 Polishing

Button-like samples were polished using grinding papers as #400, #600, #800, #1000, #1200, #1500 & #2500 at 100 RPM for 10mins each in a clockwise rotating direction Figure 20. Finally for obtaining mirror finish samples were polished using nanofiber cloths with  $3\mu\text{m}$  and  $1\mu\text{m}$  slurry of silicate at 60 RPM for 10mins each. In between changing each grind paper size samples were cleaned with ethanol.



Figure 21: Polishing on #2500

### 3.1.3 Etching

Normally for Al–Mg alloy, Keller’s reagent (2.5 ml HNO<sub>3</sub>, 1.5 ml HCl, 1 ml HF, 95 ml Distilled Water) is used [25-27]. But when observed in FESEM Al-Mg particles, Al-Fe as well as SiC particles were not visible in SC mode. Hence during the literature survey, we found out that Weck’s reagent (4 g of KMnO<sub>4</sub>, 1 g NaOH, and 100 ml of distilled water) is best suitable for observing grain boundaries as well as particles in FESEM. Hence weck’s reagent was used for observing microstructures. An example of how microstructure may vary can be seen in Figure 21.

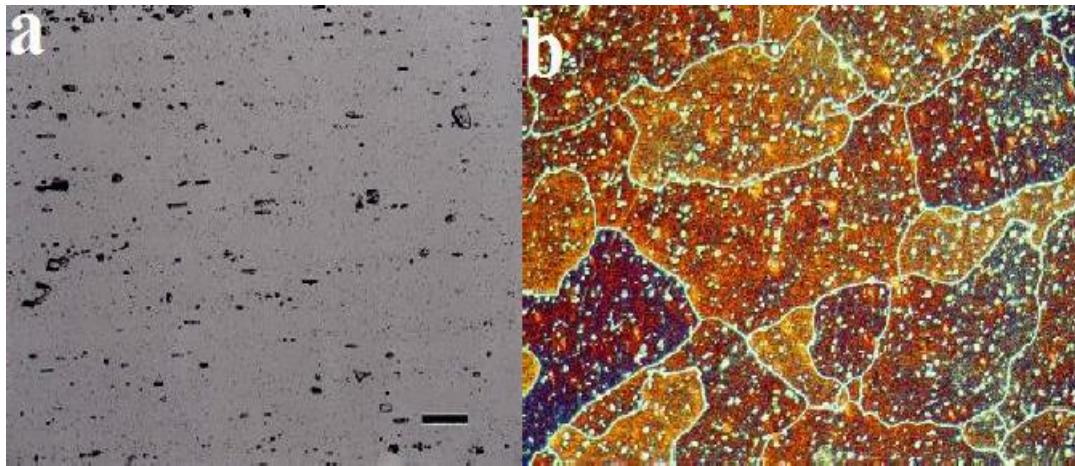


Figure 22: Optical microstructure of 6061-T6511Al alloy at 500x magnification (a) Using Keller’s reagent. (b) Using Weck’s reagent. [26]

## 3.2 Mechanical Test

### 3.2.1 Microhardness

Multiple Vickers microhardness was performed at the inner layer, interlayer, Top region, bottom region, and middle region also, after doing solution (T4) heat treatment such as T350, T500, T550, and artificial aging (T6) T500\_140. The load applied was 200g for a dwell period of 15 seconds. 8 indentations were performed at each region and final values were plotted by taking averages.

### 3.2.2 Tensile Test

Tensile tests were performed on UTM at a 1mm/min loading rate. The test specimen was horizontally prepared i.e. along the deposition direction. The tensile test specimen was prepared to have 25mm gauge length, 3mm thickness and 6mm width Figure 22. The total length of the test specimen was 100mm.

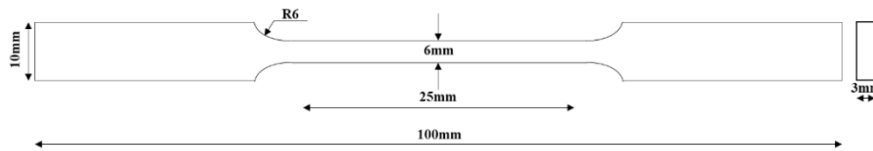


Figure 23: Flat Tensile Test Sample

### 3.3 Heat Treatment

As discussed earlier in section 2.3 micropores cause a major drawback in the mechanical properties of WAAM components. By doing heat treatment these micropores get annihilated. Also depending on the type of heat treatment there can be precipitation or solutionize strengthening. Table 5 gives the type of heat treatment performed and its processes.

Table 5: Heat Treatment Parameters

Type of Heat Treatment	Process
T350 Solutionize	350°C (12h), W.Q(100°C), 24h natural ageing
T500 Solutionize	500°C (12h), W.Q(100°C), 24h natural ageing
T550 Solutionize	550°C (12h), W.Q(100°C), 24h natural ageing
T500_140 Artificial aging	500°C (12h), W.Q, Reheat 140°C (6h,12h,24h,448h, and 120h), A.C

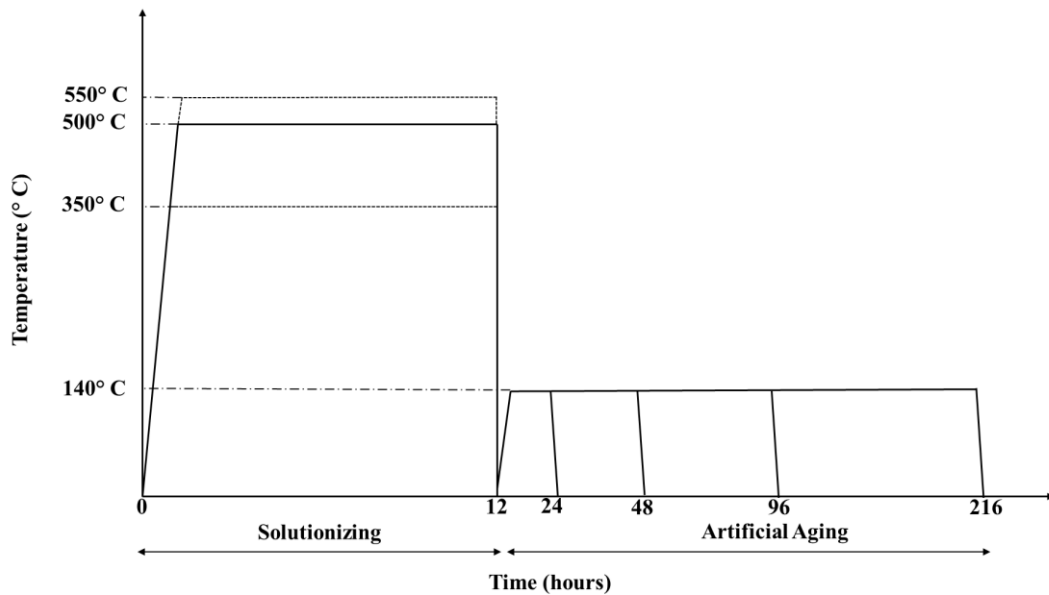
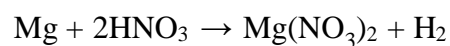


Figure 24: Heat Treatment Processes

### 3.3.1 Etching after heat treatment

The samples were polished and etched after heat treatment to examine the optical and SEM microstructures. Weck's reagent was initially used for etching, as it had produced better results before heat treatment. However, after heat treatment, the microstructure was not visible, even after varying the etching time several times. A similar phenomenon occurred with Keller's reagent. The reason for this is still unknown, but it may depend on the presence of  $\beta$ -phase.  $\text{HNO}_3$  in Keller's reagent dissolves Mg vigorously, which may explain the poor microstructure [31].



After conducting an extensive literature review and consulting ASTM etching handbooks, we experimented with various etchants. Poulton's, Keller's, and Weck's reagents yielded some results, but they were not satisfactory. Later modified Keller's reagent was used by removing  $\text{HNO}_3$  and using only HF and HCl. This worked surprisingly well. Figure 24 shows the different etchants used and the corresponding optical microstructure images.

**1.) Keller's Reagent** (2.5 ml HNO<sub>3</sub>, 1.5 ml HCl, 1 ml HF, 95 ml Distilled Water)

:-

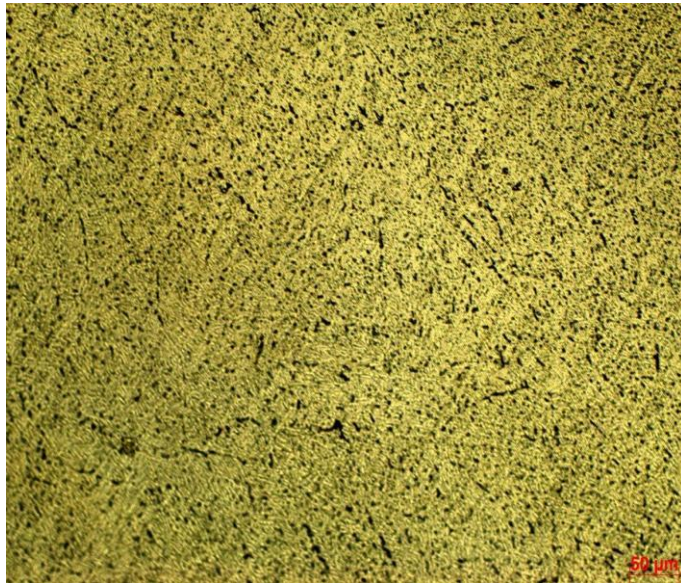


Figure 25: Optical Microstructure of heat-treated sample using Keller's Reagent

**2.) Weck's Reagent** (4 g of KMnO<sub>4</sub>, 1 g NaOH and 100 ml of distilled water):-

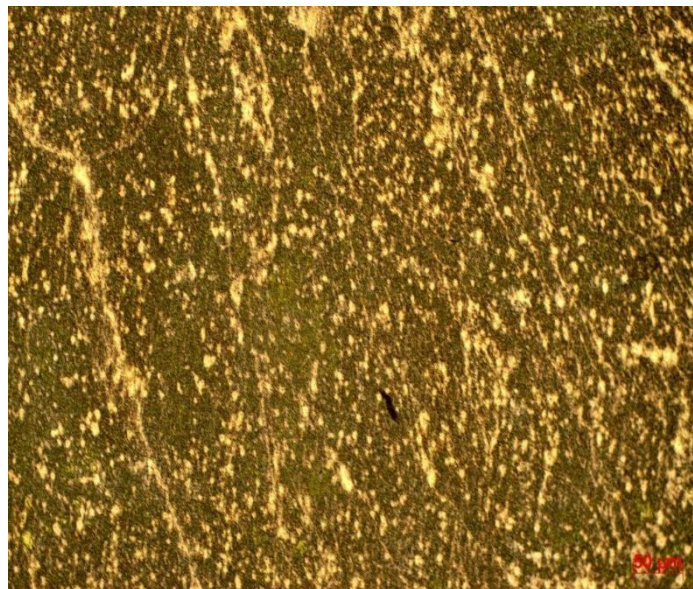


Figure 26: Optical Microstructure of heat-treated sample using Weck's Reagent

**3.) Poulton's Reagent** (12 ml HCl, 6 ml HNO<sub>3</sub>, 1 ml HF, 1 ml H<sub>2</sub>O):-

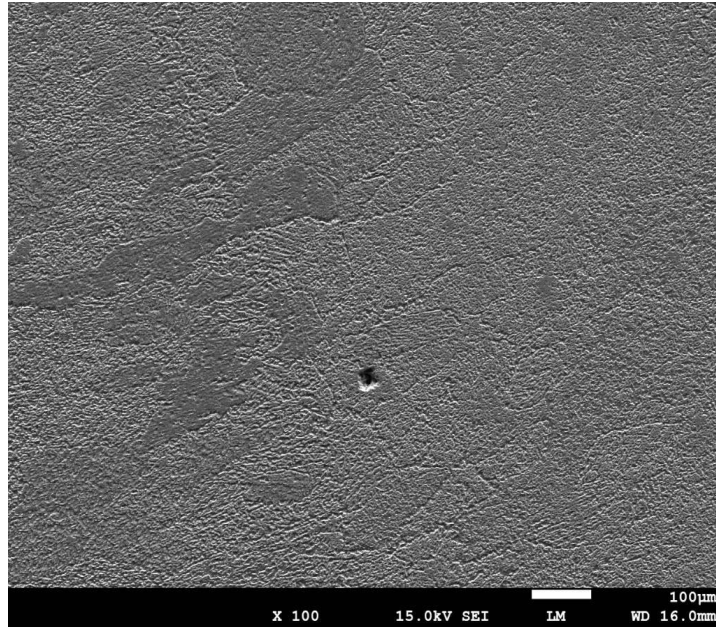


Figure 27: SEM Microstructure of the heat-treated sample using Poulton's Reagent

## Chapter 4: Results and Discussion

### 4.1 Optical Microscopy

An optical microscopy image of the as-deposited WAAM sample (longitudinal) was captured using an inverted optical microscope having 50x magnification. Figure 25a Sample was etched using Weck's reagent. We can observe inner layer regions called  $n$ ,  $n+1$ , and  $n+2$ , and the region sandwich between inner layers is called interlayers. Figure 25a (merged using two optical images) sample was etched using HF reagent which also confirms inner-layer and interlayer regions. Due to the evaporation of Mg as well as the entrapment of air from the atmosphere, we can see pores that mostly segregate near interlayer regions due to reheating from the next layer deposition (see section 2.1).

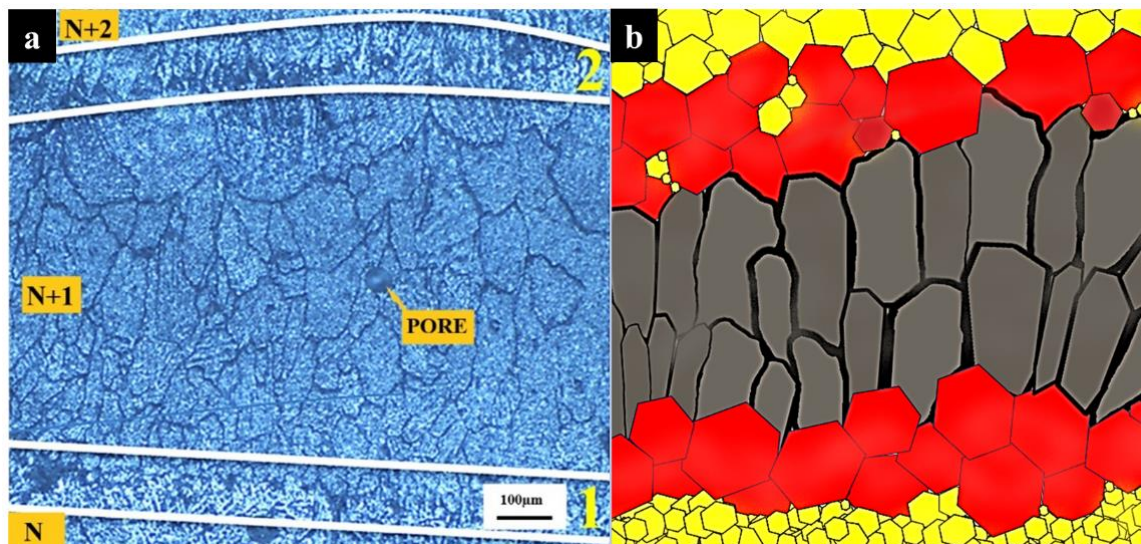


Figure 28: Optical Microscopy of as-deposited WAAM sample (longitudinal) (a) Etched with HF reagent (b) Sketch of the evolution of microstructure.

#### 4.1.1 Changes in microstructure

In the WAAM (wire arc additive manufacturing) process, there are continuous changes in microstructure due to the thermal cycle happening while depositing new layers on the pre-layers. In the early stage of WAAM pre-layer ( $n$ ) is deposited on the substrate. As there is a high temperature gradient between the pre-layer melt pool and substrate, rapid heat absorption and heat dissipation are causing a large amount of undercooling. These very fine grains will nucleate on the interface between substrate and pre-layer. The top of the pre-layer will be exposed to the atmosphere causing heat dissipation in

that direction. Hence, we can observe columnar grain growth perpendicular to the substrate or deposition direction in Figure 25b. While we deposit a new layer on the pre-layer (now solidified) still there is large amount of thermal gradient and hence fine grains will nucleate in the region of the interface also known as the interlayer. As the heat dissipates through the pre-layer there is a coarsening of grains at the top region of the pre-layer. Also, the heat dissipation from the pre-layer top of the new layer will do coursing of fine grains at the bottom part of the new layer Figure 25b. There is rapid heat dissipated through the new layer, due to the exposed surface to the atmosphere on top of the new layer. This will again cause columnar grain growth perpendicular to the substrate or deposition direction. This thermal cycle will keep on happening till we finish depositing metal to make our component. Therefore, we can say that there will be three types of grains in the WAAM sample, (1) fine grains which will grow in interlayers (Yellow-Hexagon), (2) Coarse Equaxe-Grains (Red-Hexagonal) which will grow just below and above the interlayer, (3) Columnar-Grains in the region of the inner layer (Gray Strips) Figure 25b.

#### **4.1.2 Microstructure after Heat Treatment**

T4 heat treatment at 500 °C was performed on button samples. Optical microstructures were taken using HF reagent after etching for about 55s Figure 29. We can observe that unlike the microstructure of the as-deposited sample which had Course, fine equiaxed grains as well as some columnar grains in between the deposition layers, there was coursing of equiaxed grains in heat-treated samples. Also, we observed that the number of columnar grains decreased significantly mainly due to artificial aging at 200 °C. When heat treated sample was scanned under an optical microscope no inter-layers were found. This is because heat treatment causes grain refinement and homogenization of the microstructure [32].

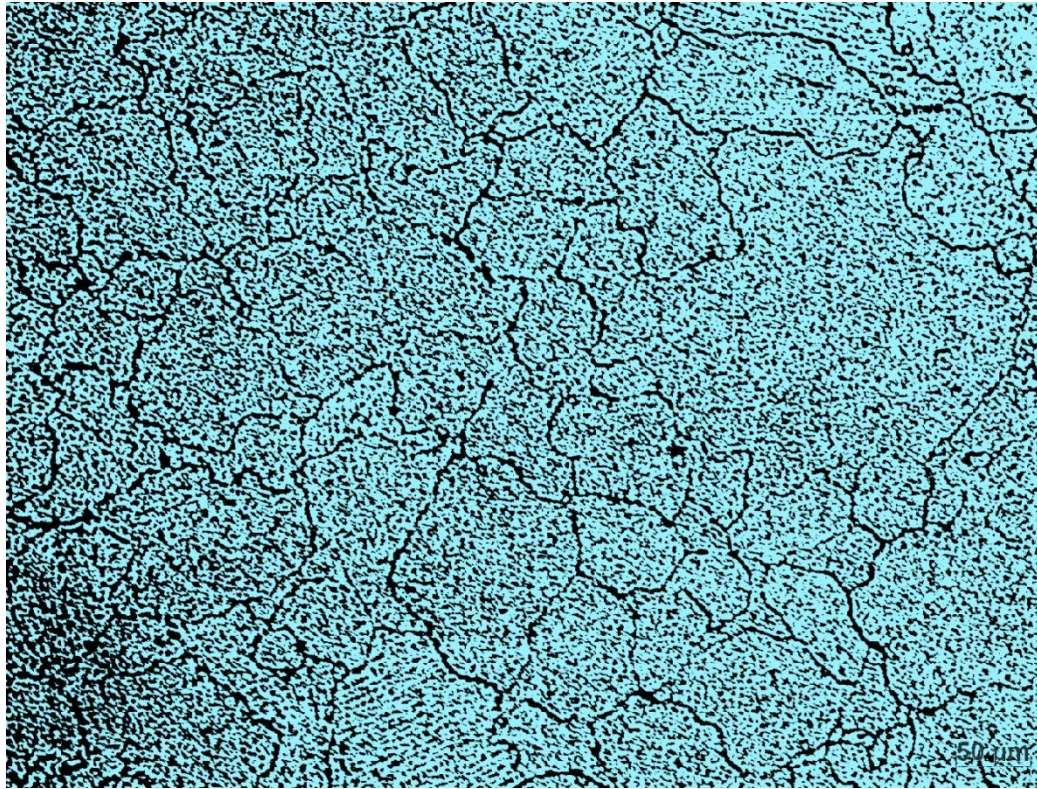


Figure 29:Optical Microstructure of heat-treated sample.

## 4.2 EDS Analysis

The as-deposited scanning electron micrograph of AA5356 and their respective elemental distribution are shown in Figure 30a. The elemental distribution was performed using an EDS analysis. From the micrograph, various particles with different morphologies are observed, which include dull globular-shaped particles (Red arrow a), needle-shaped particles (Yellow arrow b), and shiny globular-shaped particles (Black arrow c). The EDS analysis in Figure 30a (spectrum a) indicates that the dull globular particles predominantly comprise the Al-Mg phase, but it could not be confirmed as an  $\text{Al}_3\text{Mg}_2$  secondary phase. As reported by Yanfei Geng et al. [36], the  $\text{Al}_3\text{Mg}_2$  secondary phase particle appears in the microstructure with a size in nanometers, which can be successfully traced using TEM microscopy. However, the x-ray diffraction profile shown in Figure 27 confirms the existence of the  $\text{Al}_3\text{Mg}_2$  phase in addition to the primary  $\alpha$ -Al matrix phase in AA5356 alloy. On the other hand, iron (Fe) was identified as the second major element in Figure 27a (spectrum b), it appeared in the micrograph as a needle-shape Al-Fe phase (Yellow arrow b). In addition, there is also a possibility of the existence of the Si-C phase in the micrograph, Figure 27a

(spectrum c). Although an Al-Fe and Si-C phase is conceivable, no known peaks were detected in the XRD analysis.

To illustrate the effect of solution heat treatment on the microstructure of as-deposited AA5356 alloy, the T500 solution heat-treated bottom sample has been considered. The microstructure of the T500 sample is demonstrated in the micrograph, shown in Figure 27b. On heat treatment, most of the secondary phases are dissolved into the Al matrix. The EDS analysis confirms the dissolution of these phases and the evolution of some impurities as indicated by arrows black a and red b. The absence of x-ray diffraction peaks associated with the  $\text{Al}_3\text{Mg}_2$  phase on heat treatment further confirms its complete dissolution, Figure 28. Since the SiC phase is brittle and can compromise the ductility of the deposited alloy, their reduction on heat treatment is favorable for the mechanical properties of the material. Furthermore, the Al-Fe phase that appeared in the as-deposited condition can act as a stress concentrator due to its needle-shaped morphology, which could weaken the strength of the deposited alloy by initiating crack formation. The employed heat treatment eliminates the adverse effect of the needle-shape Al-Fe phase by dissolving it completely into the Al matrix.

In addition, an attempt has been made to understand the effect of precipitation strengthening on the microstructure evolution and mechanical properties of the alloy. In this context, the bottom sample of the as-deposited alloy was further subjected to a heat treatment process named artificial aging (T6). The backscattered electron micrograph of the T6 heat-treated sample (140°C for 12 h) is shown in Figure 27c. The BSE (Backscattered Electron) imaging technique was specifically utilized to identify  $\text{Al}_3\text{Mg}_2$  secondary phase based on differences in contrast. In the micrograph shown in Figure 5C, the fine bright particle precipitates were observed (indicated by black arrow a), composed of Al-Mg-Fe element (Spectrum a). In addition, a continuous network of bright regions was identified as none other than the matrix Al-Mg phase (indicated by yellow arrow b). The very fine particles of the  $\text{Al}_3\text{Mg}_2$  secondary phase are still not traceable in the microstructure even after T6 heat treatment, but their existence was successfully confirmed by the x-ray diffraction analysis, Figure 28.

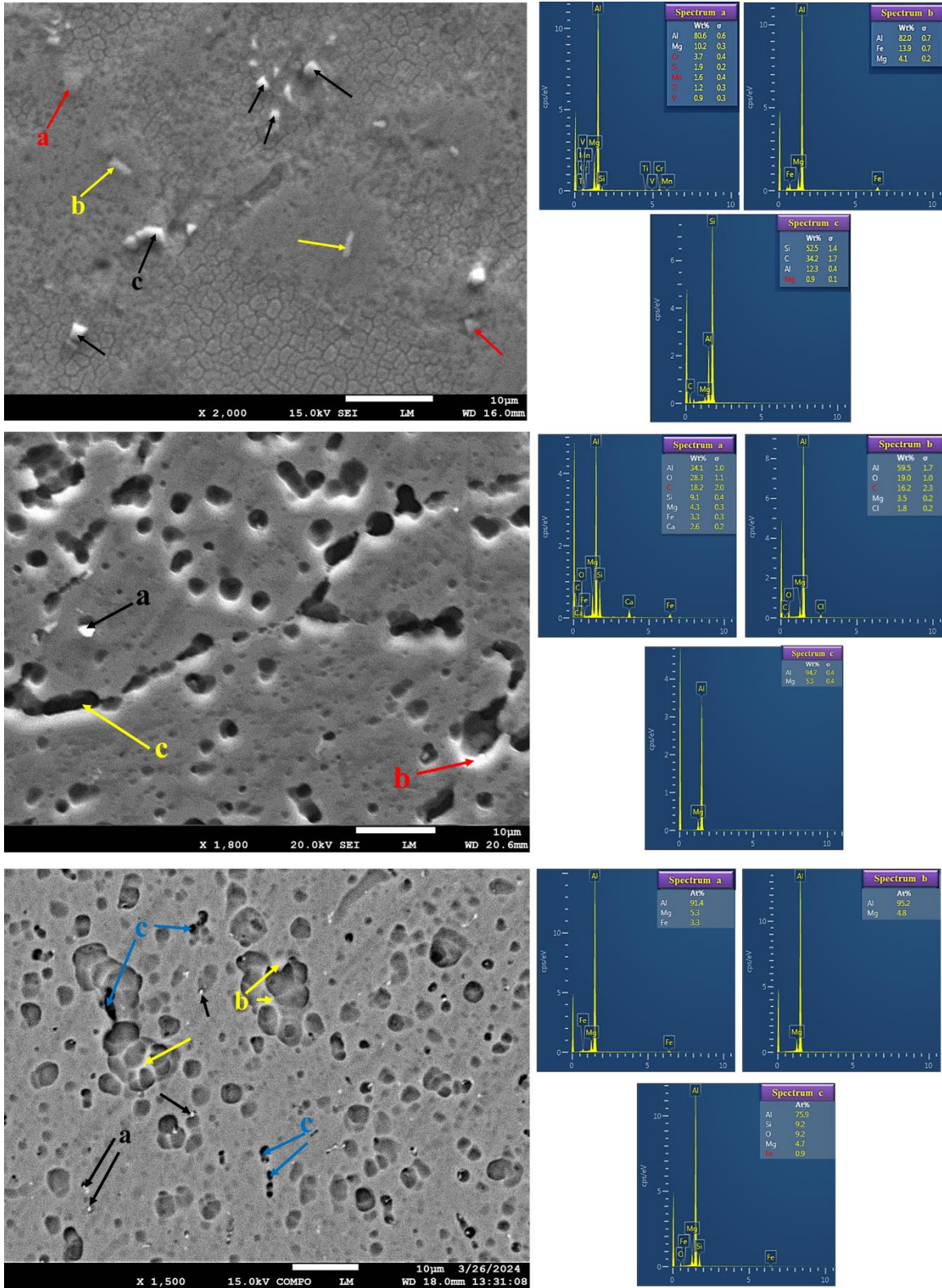


Figure 30: SEM micrograph and EDS analysis of (a) As-deposited sample, (b) T500 heat treated, (c) T6 heat treated at 140 °C for 12h

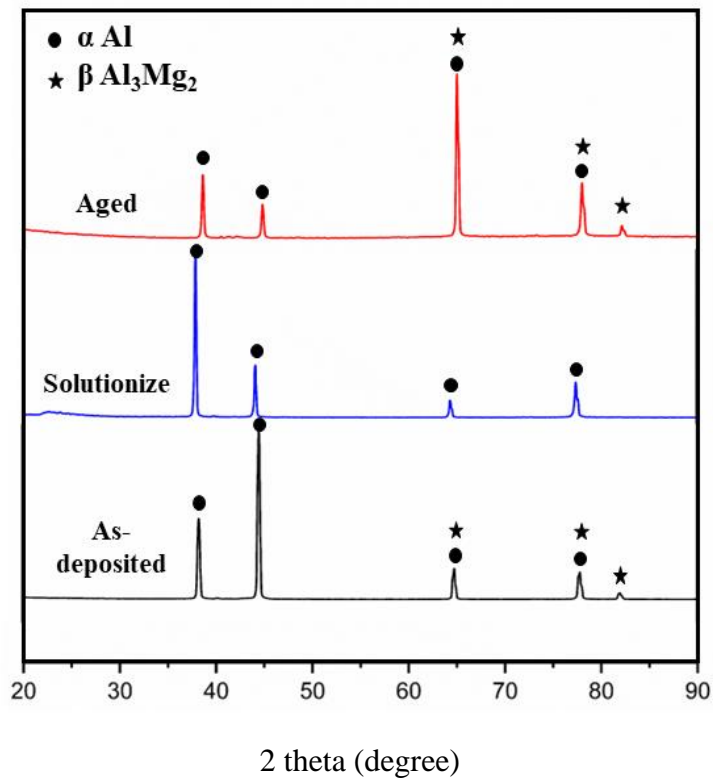


Figure 31: XRD analysis for Al Mg alloy.

### 4.3 Grain size distribution.

The microstructure evolution in the building direction during the deposition is attributed to heat dissipation. Cold Metal Transfer (CMT) based additive manufacturing (AM) offers a flexible and rapid wire arc additive manufacturing (WAAM) process. The microstructure resulting from the CMT-WAAM process is mainly attributed to heat dissipation. The microstructure consists of equiaxed grains, especially after heat treatment procedures. Equiaxed grain size increases from bottom to top for both as-deposited and heat-treated samples. This increase in grain size may be due to heat dissipation from the wall and the substrate. Generally, two modes of heat transfer are involved: conduction (from the bottom region of the wall to the substrate) and convection (from the wall and substrate to the surrounding atmosphere). Conduction, a faster heat transfer mode, results in rapid heat dissipation from the bottom region of the

wall to the substrate, leading to smaller equiaxed grains in the bottom region. Moreover, Equation (1) indicates that heat dissipation by convection from the substrate outpaces that from the wall regions, primarily because of the substrate's larger surface area.

$$\mathbf{q} = h_c A \Delta T \quad (1)$$

Here,  $q$  = heat transferred per unit time (W),  $A$  = heat transfer area of the surface ( $m^2$ ),  $h_c$  = convective heat transfer coefficient ( $W / (m^2 \text{ } ^\circ C)$ ), and  $\Delta T$  = temperature difference between the surface and surrounding atmosphere ( $^\circ C$ ).

Hence, it is observed that the trend of grain size distribution involves an increase in average grain size from the bottom to the middle region, reaching its maximum at the top. Figure 32 shows that the data indicates an average grain size of 35.4  $\mu m$  at the bottom, progressively rising to 50.4  $\mu m$  in the middle region, and has a maximum average grain size of 56.3  $\mu m$  in the top region.

After performing T4 heat treatment on samples from the bottom, middle, and top regions, the same trend in grain size was observed as in the as-deposited condition. Specifically, the average grain size increased from the bottom region to the top region Figure 33. In the top region, the grain size increased from 56.29  $\mu m$  to 81.84  $\mu m$ , followed by an increase from 50.46  $\mu m$  to 72.63  $\mu m$  in the middle region, and finally, an increase from 34.55  $\mu m$  to 60.84  $\mu m$  in the bottom region.

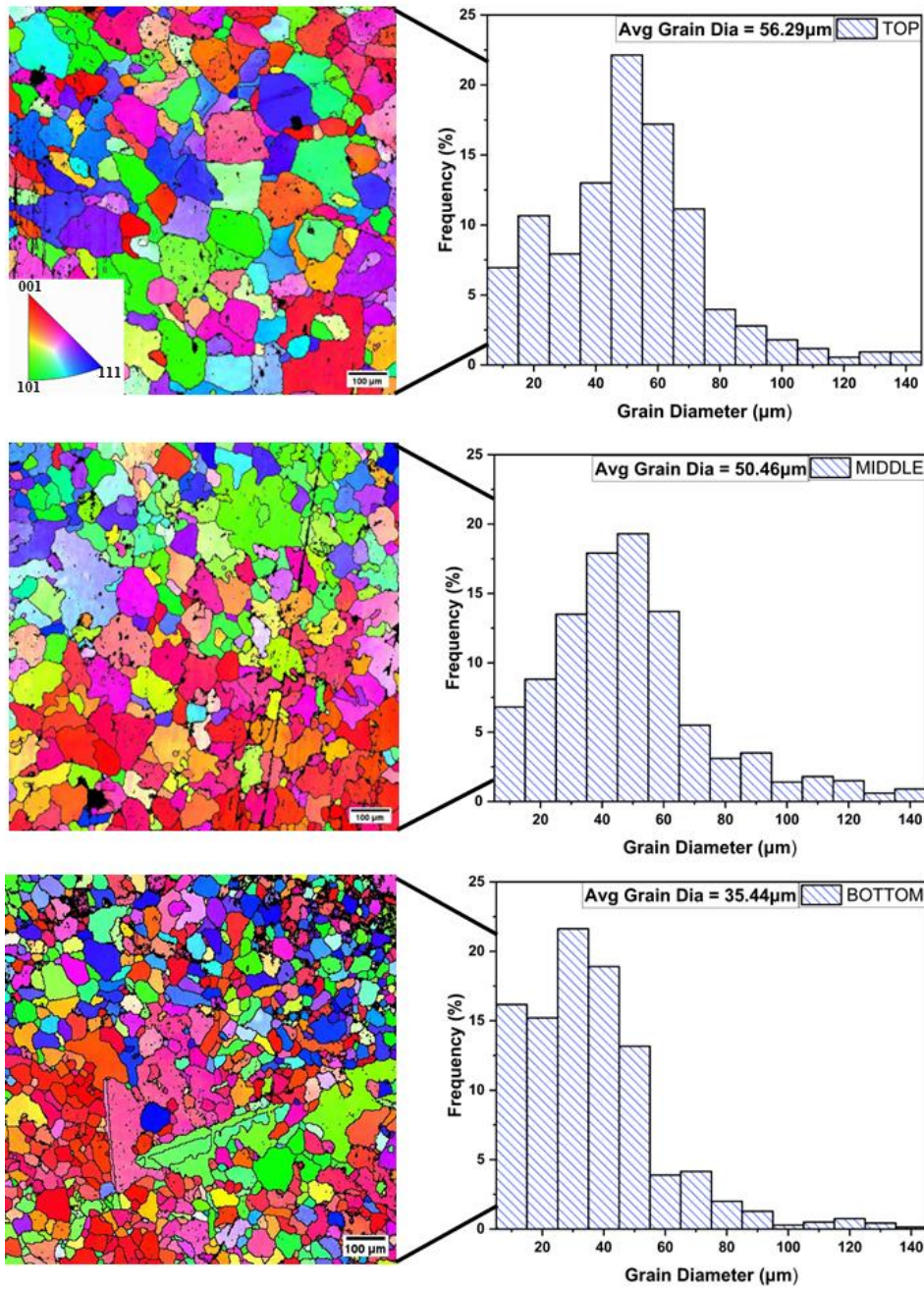


Figure 32: EBSD analysis of As-deposited samples from top, middle, and bottom regions

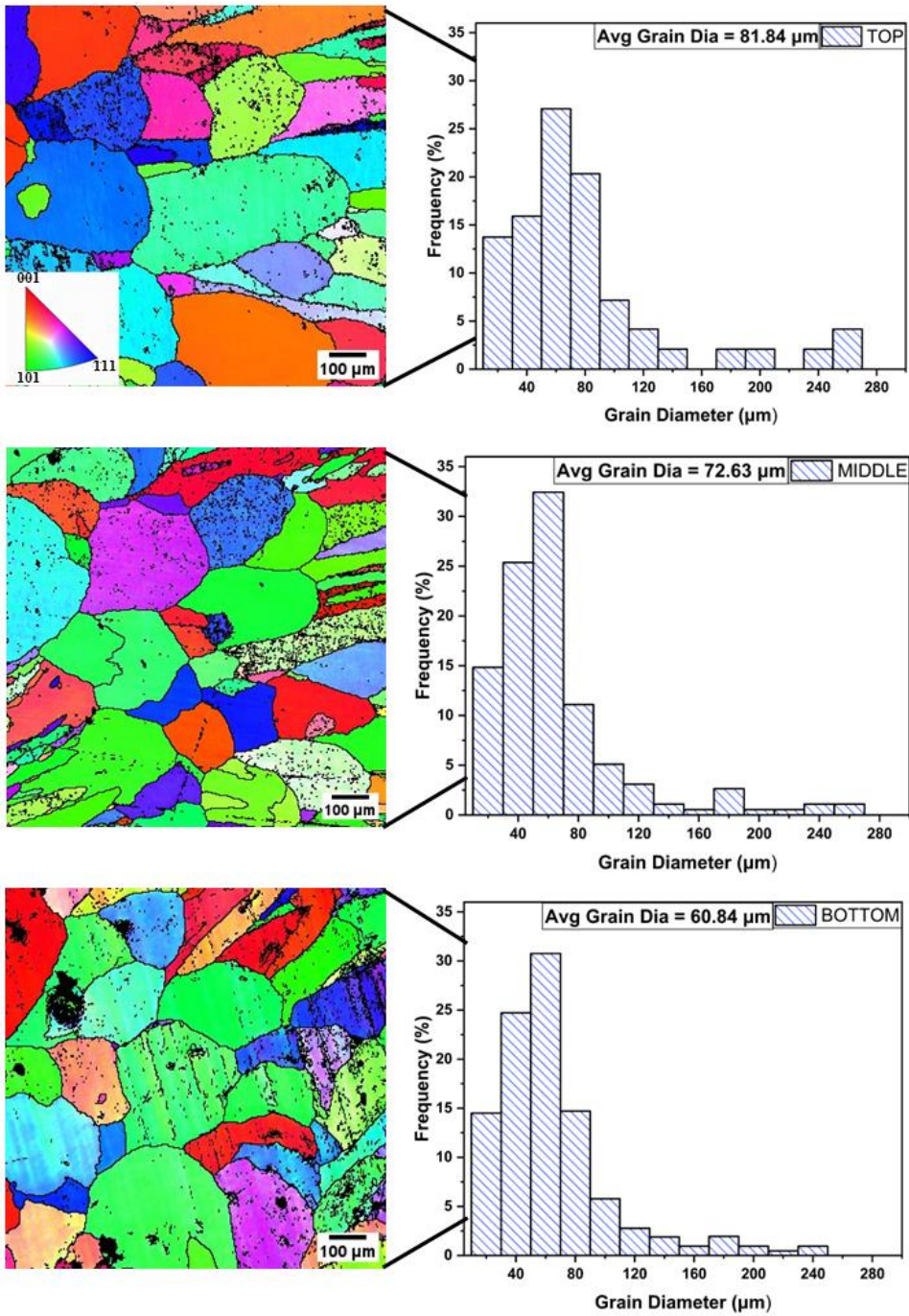


Figure 33: EBSD analysis of T500 samples from top, middle, and bottom regions

#### 4.4 Hardness Analysis: -

The microhardness measurements were performed on the deposited wall in three different regions i.e., bottom, middle, and top regions. The measurement was done with the applied load of 200 gf for 15 s dwell time. Each microhardness value reported in the present study is an average of a total of 8 indentations.

In the case of as-deposited samples, the average microhardness value at the bottom was estimated to be 82.83 HV, decreasing to 77.65 HV in the middle region. The lowest microhardness value estimated in the top region was 71.73 HV. On the basis of the higher microhardness value obtained in the bottom region, the sample from the bottom region was further considered to investigate the effect of T4 and T6 heat treatment on microhardness value.

On solution (T4) heat treatment at 300 °C, 500 °C, and 550 °C different temperatures, the average estimated microhardness values of the sample are as follows: T300 - 92.09 HV, T500 - 101.12 HV, and T550 - 97.96 HV. The specimen on T500 heat treatment shows the highest microhardness value and, therefore, it is further considered for additional aging (T6) heat treatment for 6h, 12h, 24h, 48h, and 120h time periods. The estimated microhardness values are 83.11333 HV (6h), 95.02167 HV (12h), 79.60333 HV (24h), 70.80167 HV (48h) and 64.135 HV (120h). The specimen subjected to T6 heat treatment for 12h resulted in the highest microhardness value. In summary, from the experimental observation, the estimated microhardness values for the bottom sample follow the trend  $HV_{T4} > HV_{T6} > HV_{As-deposited}$ .

Similarly, the microhardness values in the middle and top regions of the deposited wall are also estimated by following the same trend as discussed above. The obtained microhardness values in all three regions are illustrated in Table 4. In addition, the plots demonstrating the change in behavior of the microhardness values are shown in Figure 30.

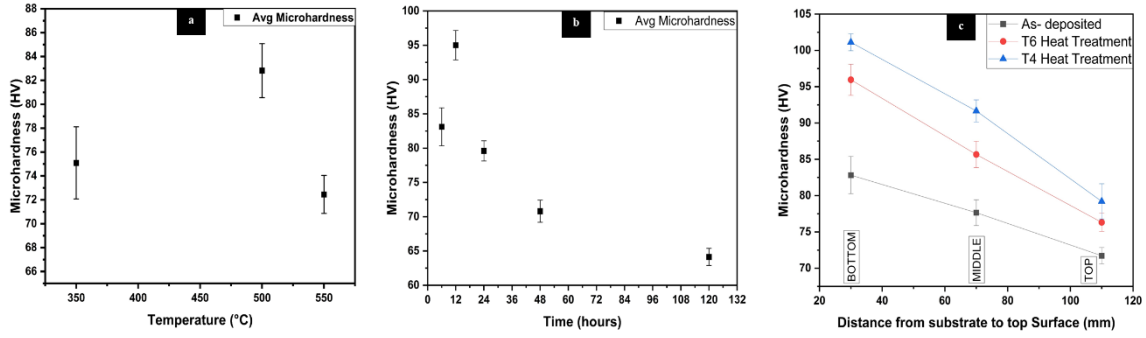


Figure 34: Microhardness distribution in (a) T350, T500, and T550 on top samples, (b) T6 heat treatment on bottom samples for 6-120h, and (c) Top, Middle, and Bottom samples.

Table 6: Vicker microhardness values of the AA5356 alloy in different regions at specified conditions.

	Bottom (HV)	Middle (HV)	Top (HV)
<b>As-deposited</b>	82.83	77.65	71.73
<b>T4 heat treated</b>	101.12	91.66	79.20
<b>T6 heat treated</b>	95.955	85.67	76.32

#### 4.5 Tensile Test: -

As discussed above, the microhardness value associated with the bottom region sample was observed to be superior compared to the middle and top regions. Further, subjecting the bottom region sample to T4 and T6 heat treatment, a significant improvement in the microhardness value is observed in the case of the T4 heat-treated sample. Therefore, in the present study, the specimen for the tensile test was considered from the bottom region under two different conditions, i.e., as-deposited and solution (T4) heat-treated. In addition, based on deposited wall orientation, the tensile test specimens are extracted in two different directions, such as horizontal (deposition) direction and vertical (building) direction, as shown in Figure 2a.

The tensile test in each condition was carried out with a strain rate of  $0.001 \text{ s}^{-1}$  at room temperature. To ensure repeatability, the tensile test was carried out on 3 specimens for each condition. The estimated tensile test results are illustrated in Table 5. In addition, the respective tensile curve plots are demonstrated in Figure 31.

In the case of as-deposited specimens, the yield strength (YS) was approximately 105.21 MPa, and the ultimate tensile strength (UTS) was about 162.82 MPa in the horizontal (deposition) direction. In contrast, in the vertical (building) direction, the YS was measured at 89.53 MPa, and the UTS was about 148.84 MPa, as shown in Figure 31. From the observations, it is concluded that the horizontal specimens exhibit higher yield and ultimate tensile stress compared to vertical specimens. Specifically, in the case of elongations, an opposite trend was observed. The elongation in the vertical direction was measured at 6.14%, whereas in the horizontal direction, it was observed to be 4.91%, Figure 31a. This behavior may be attributed to the presence of columnar grains in the building (vertical) direction.

Following T4 heat treatment, there was a slight increase in yield strength (YS) and a noticeable enhancement in ultimate tensile strength (UTS) and elongation for both horizontal and vertical directions. In the horizontal direction, YS was measured at 108.37 MPa (3% increase from the as-deposited state), UTS at 206.37 MPa (a 21.1% increase from the as-deposited state), and elongation at 12.87% (61.8% increase from the as-deposited state). Similarly, for vertically oriented specimens, YS was recorded as 92.72 MPa (3.4% increase from the as-deposited state), UTS as 207.28 MPa (28.2% increase from the as-deposited state), and elongation as 17.96% (66% increase from the as-deposited state) Figure 31b.

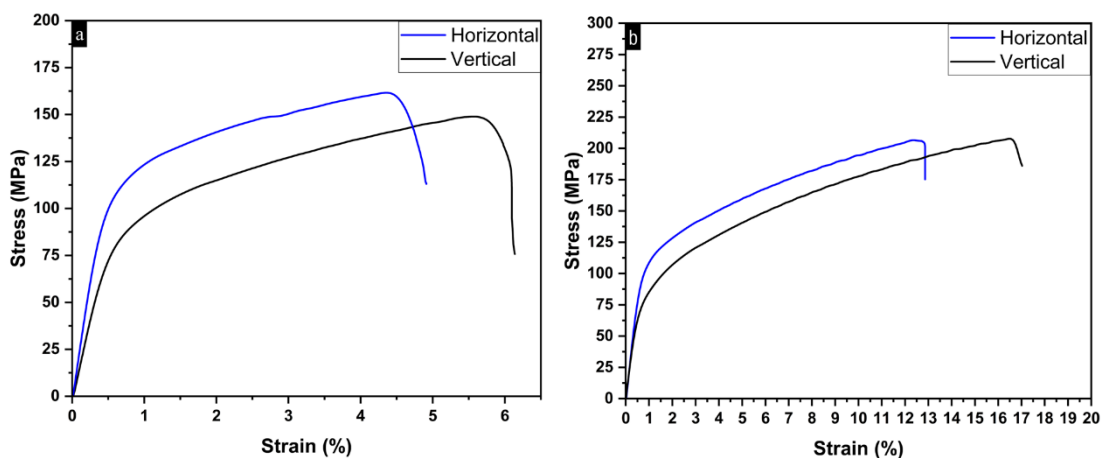


Figure 35: Tensile properties in horizontal and vertical of (a) As-deposited and (b) T500 heat-treated conditions.

Table 7: Tensile strength values of the AA5356 alloy in different regions at specified conditions.

	<b>Direction</b>	<b>Yield Strength <math>\sigma_y</math>, (MPa)</b>	<b>Ultimate tensile strength <math>\sigma_{max}</math>, (MPa)</b>	<b>Elongation (%)</b>
<b>As- deposited</b>	Horizontal	105.21 $\pm$ 2.8	162.82 $\pm$ 2.1	4.91 $\pm$ 1.4
	Vertical	89.53 $\pm$ 4.2	148.84 $\pm$ 2.7	6.14 $\pm$ 4.4
<b>T4 Heat Treated</b>	Horizontal	108.37 $\pm$ 3.1	206.37 $\pm$ 1.8	12.87 $\pm$ 1.9
	Vertical	92.72 $\pm$ 5.7	207.28 $\pm$ 3.0	17.96 $\pm$ 4.7

Ultimate tensile strength in the horizontal direction was around 162.8 MPa while in the vertical direction, it was about 148.8 MPa. This Change in ultimate tensile strength is due to the pores at the interfaces between each deposited layer, which can reduce the interlayer bonding and act as stress concentrators. The pores are more likely to form in the vertical direction than in the horizontal direction, because of the lower heat input and higher cooling rate in the vertical direction

#### **4.6 Effect of heat treatment on mechanical properties of WAAM**

##### **AA5356 alloy**

During T4 heat treatment processes such as T350, T500, and T550, two distinct strengthening mechanisms operate within AA5356 alloy samples [22].

The first mechanism is solute solution strengthening ( $\sigma_{SSS}$ ), wherein magnesium (Mg) atoms dissolve into the Aluminum (Al) matrix, acting as point defects that hinder the movement of dislocations, thereby strengthening the alloy (see Equation 2) [23].

$$\sigma_{SSS} = \sigma_{pure} + HC^n \quad (2)$$

The second mechanism is grain boundary strengthening ( $\sigma_{\text{gbs}}$ ). According to the Hall-Petch equation (see Equation 3), the strength of the alloy is inversely proportional to the grain size [24]. After performing T4 heat treatment, the average grain size in the bottom region increased from 35.4  $\mu\text{m}$  to 60.8  $\mu\text{m}$  (see Figure 29 and Figure 30). Consequently, this increase in grain size leads to a reduction in the strength of the material (see Equation 3).

$$\sigma_{\text{gbs}} = \frac{K}{\sqrt{d}} \quad (3)$$

For T6 heat treatment processes, precipitation strengthening ( $\sigma_{\text{ps}}$ ) and grain growth mechanisms operate within the AA5356 alloy sample. Upon performing T6 heat treatment Mg element precipitates out to form  $\beta$ -Phase ( $\text{Al}_3\text{Mg}_2$ ) which hinders the motion of dislocations thereby increasing the strength of the alloy (see equation 4).

$$\sigma_{\text{ps}} = \sqrt{3} \frac{Gb}{\rho} \quad (4)$$

Based on microhardness results which were reported in section 4.1, the influence of solid solution strengthening, grain boundary strengthening, and precipitation strengthening varies in their effectiveness for enhancing strength. Solid solution strengthening assumes the most crucial role, followed by grain boundary strengthening, and precipitation strengthening, respectively. In T500 alloys, with average grain sizes around 60.8  $\mu\text{m}$  in the bottom region, the dissolution of the  $\beta$  phase into the  $\alpha$ -Al matrix results in a reduction of grain boundary strengthening and precipitation strengthening. However, it is precisely due to this dissolution of the  $\beta$  phase into the  $\alpha$ -Al matrix that the increase in solid solution strengthening outweighs the decrease in grain boundary strengthening and precipitation strengthening. Consequently, T500 alloys achieve their highest strength. After performing the T4 heat treatment, a significant increase in elongation was observed in both the horizontal and vertical directions. This variation in elongation properties can be attributed to the brittle-to-ductile transition induced by the T4 heat treatment (see Figure 32s).

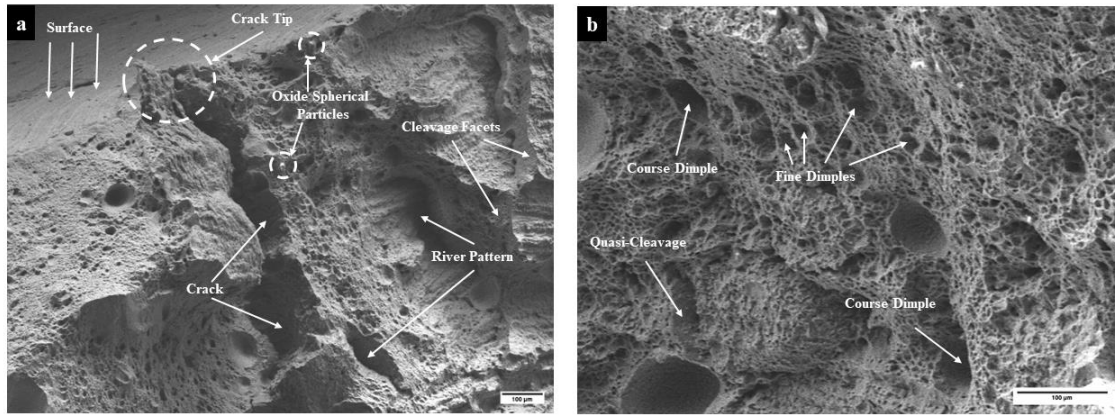


Figure 36: SEM fractography of (a) as-deposited sample, (b) T500 heat-treated sample.

#### 4.7 Creep Test: -

The creep test specimens underwent constant load creep testing within a temperature of 170 °C, 190 °C, 200 °C, and 210 °C. The tests were conducted at applied stress values of 60 MPa, 65 MPa, 75 MPa, and 80 MPa, using a single lever Star Testing Machines (STS) creep testing machine with a lever ratio of 20:1. The creep specimens were heated at the desired temperature using a three-zone heating furnace externally attached with the STS machine. An extensometer with the help of a dial gauge measured strain in the gauge length (G.L). Changes in the strain readings were saved in the data logging system. Strain value data were taken at every 1-minute interval up to the fracture of the creep specimen.

Figure 33a illustrates the typical tensile creep curves (strain% vs time plots) for the WAAM AA5356 Al alloy, tested within a temperature range of 170–210 °C and a stress range of 60–80 MPa. These curves exhibit the three well-defined stages of creep i.e. a primary stage for a short duration, a secondary stage with a virtually constant strain rate, and a tertiary stage. Figure 33b shows the strain rate vs. time plots under various testing conditions, illustrating the creep behavior of the WAAM AA5356 Al alloy. For all the creep curves, the trend shows that the strain rate decreases during the primary stage, remaining almost constant during the prolonged secondary stage, and increasing during the tertiary stage. As expected, the strain rate increases with higher applied loads and temperatures. The steady-state strain rates vary from a minimum of  $6.03E^{-09}$  ( $s^{-1}$ ) under 60 MPa stress at 170°C to a maximum of  $4.78E^{-07}$  ( $s^{-1}$ ) under 80 MPa stress at 200 °C.

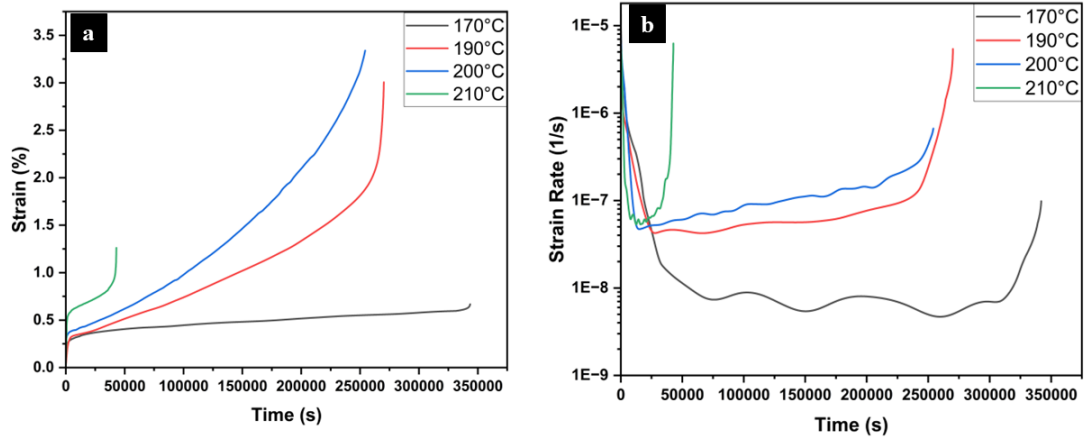


Figure 37: Creep curves of WAAM AA5356 Al alloy for (a) Strain vs Time, (b) Strain rate vs Time.

To identify the governing creep mechanism, the stress exponent ( $n$ ) and activation energy ( $Q$ ) were calculated under various test conditions. The values of  $n$  and  $Q$  differ depending on the operative creep mechanism. The slopes of the lines relating  $\ln$  (strain rate) to the inverse of temperature were used to calculate the apparent activation energy ( $Q$ ), which was determined to be 130 kJ/mol (see Fig 34a). Similarly, the slopes of the lines relating  $\ln$ (strain rate) to  $\ln$ (stress) were used to calculate the creep exponent ( $n$ ), which was found to be 5.27 (see Fig 34b). These creep parameters suggest that the creep failure mechanism is likely due to dislocation climb.

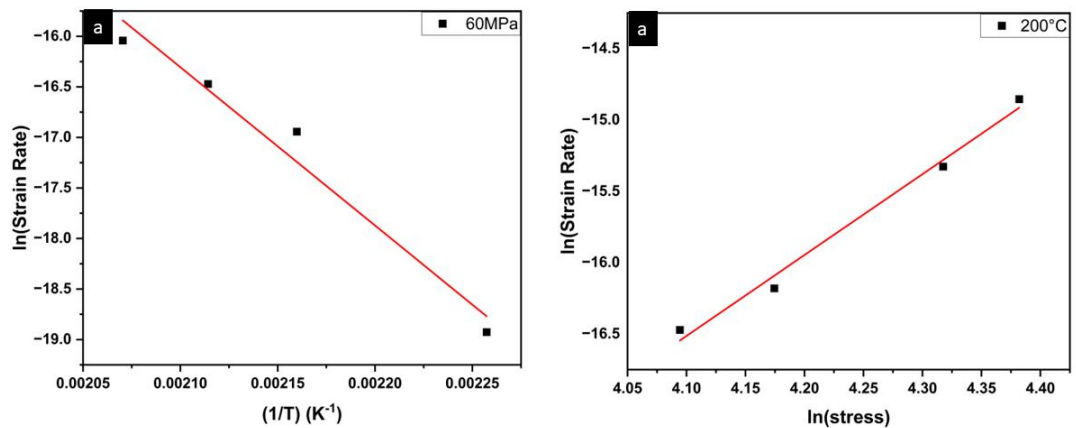


Figure 38: Relationship between (a)  $\ln$  (strain rate) and inverse of temperature, (b)  $\ln$  (strain rate) and  $\ln$ (stress)

The microstructure after creep was examined at a depth of 2-3mm from the free surface. Fig 39a indicates that creep crack initiation is likely to occur in the interlayer region,

possibly due to the higher concentration of defects present there. Crack propagation was observed to occur through the triple points at grain boundaries Fig 39b. Crack propagation has been observed to occur through the triple points at grain boundaries. The presence of  $\beta$ -phase ( $\text{Al}_3\text{Mg}_2$ ) particles near the intergranular regions [24] may contribute to creep crack propagation through these intergranular regions.

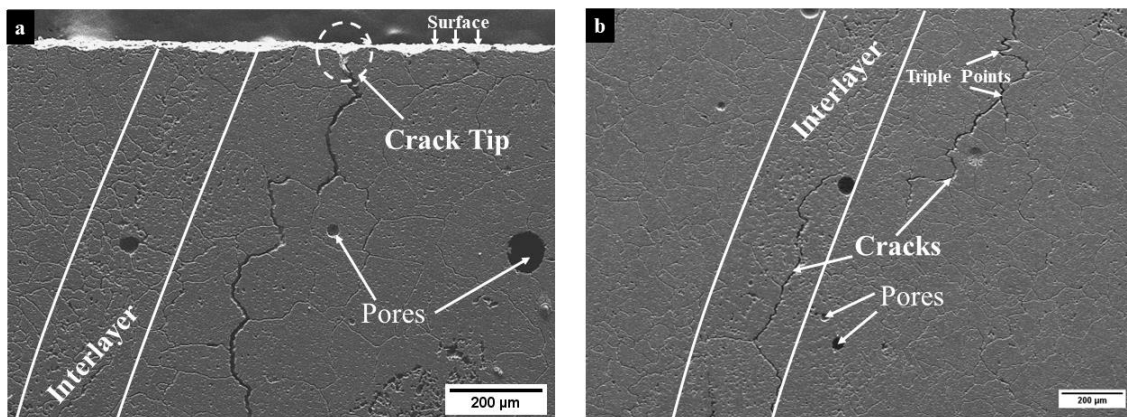


Figure 39: Post creep microstructure of (a) near surface, (b) at depth of 2-3mm.

## Conclusions

- The Literature survey studied the mechanical strength of WAAM components, which lies between the cast and extruded or rolled components.
- There are majorly three major types of grains in WAAM components i.e. (a) Fine grains, (b) Coarse equiaxed grains, and (c) Columnar grains.
- EDS analysis showed the Al-Mg phase has globular morphology which helps in increasing the mechanical properties of the component.
- $\beta$ -Phase ( $Al_3Mg_2$ ) in as-deposited and T6 heat-treated samples was confirmed using XRD analysis.
- Various heat treatment processes were studied and finally, T4 heat treatment at 500°C was confirmed for improving hardness and tensile strength for the WAAM samples.
- EBSD analysis illustrated grain size increment from 56  $\mu m$  to 75  $\mu m$ .
- Based on the creep test results, apparent activation energy ( $Q_c$ ) was calculated as 130.2 (KJ/mol) and creep exponent (n) as 5.67 which suggests the dislocation climb could be the dominating creep mechanism operating for applied load and temperature range.

## **Future Work**

- Effect of T4 and T6 heat treatment on creep behavior for WAAM 5356 Al alloy

## REFERENCES

1. Ralph, Baker. "Method of making decorative articles." U.S. Patent No. 1,533,300. 14 Apr. 1925.
2. Wang, Jiankun, et al. "Arc Additively Manufactured ER5356 Aluminum Alloy with Cable-Type Welding Wire: Microstructure and Mechanical Properties." *J. of Materi Eng and Perform* 30, vol. 30, no. 10, Springer Science+Business Media, May 2021, pp. 7472–78.
3. Raut, L.P., Taiwade, R.V. *Wire Arc Additive Manufacturing: A Comprehensive Review and Research Directions.*, 4768–4791 (2021).
4. J.D. Spencer, P.M. Dickens, and C.M. Wykes, *Rapid Prototyping of Metal Parts by Three-Dimensional Welding*, *Proc. Inst. Mech. Eng. Part B J. Eng. Manuf.*, 1998, 212, p 175–182.
5. Y.M. Zhang, Y. Chen, P. Li and A.T. Male, *Weld Deposition-Based Rapid Prototyping: A Preliminary Study*, *J. Mater. Process. Technol.*, 2003, 135, p 347–357.
6. Y. Nie, P. Zhang, X. Wu, G. Li, H. Yan and Z. Yu, *Rapid Prototyping of 4043 Al-Alloy Parts by Cold Metal Transfer*, *Sci. Technol. Weld. Join.*, 2018, 23, p 527–535.
7. M.R.U. Ahsan, A.N.M. Tanvir, G.J. Seo, B. Bates, W. Hawkins, C. Lee et al., *Heat-Treatment Effects on a Bimetallic Additively-Manufactured Structure (BAMS) of the Low-Carbon Steel and Austenitic- Stainless Steel*, *Addit. Manuf.*, 2020, 32, p 101036.
8. P.O. Noble, *Method and Apparatus for Electric Arc Welding*, U.S. Patent 1898060, (1933)
9. R. Carpenter Otis, H. J. K., "Method and Apparatus for Metal Coating Metal Pipes by Electric Fusion," U.S. Patent 2427350, (1947)
10. White W. *Pressure Roller and Method of Manufacture*, U.S. Patent 3156968, (1964)
11. H. Brandi, *Method of Making Large Structural One-Piece Parts of Metal*,
12. *Particularly One-Piece Shafts*, U.S. Patent 3985995, (1976)

13. R. Acheson, Automatic welding apparatus for weld build-up and method of achieving weld build-up,  
U.S. Patent 4952769 (1990)
14. Y.A. Song, S. Park, D. Choi and H. Jee, 3D Welding and Milling: Part I-a Direct Approach for Freeform Fabrication of Metallic Prototypes, *Int. J. Mach. Tools Manuf.*, 2005, 45, p 1057–1062.
15. G. Anzalone, C. Zhang, B. Wijnen, P. Sanders, J. Pearce, et al., A Low-Cost Open-Source Metal 3-D Printer, *IEEE Access*, IEEE, Vol. 1, pp. 803–810 (2013).
16. J.S. Gaddes, *Parametric Development of Wire 3D Printing* (2015)
17. Thomas, Douglas. (2017). *Economics of Additive Manufacturing*.
18. Ladani, L.; Sadeghilaridjani, M. Review of Powder Bed Fusion Additive Manufacturing for Metals. *Metals* **2021**, *11*, 1391.
19. Knezović, N., Topić, A. (2019). Wire and Arc Additive Manufacturing (WAAM) – A New Advance in Manufacturing. In: Karabegović, I. (eds) *New Technologies, Development and Application. NT 2018. Lecture Notes in Networks and Systems*, vol 42. Springer, Cham.
20. WAAM explained - Wire Arc Additive Manufacturing - RAMLAB. (n.d.). April 14, 2023,
21. J.R. Davis, ‘Aluminum and Aluminum Alloys ‘ : Alloying: Understanding the Basics, p351-416
22. Sunny, K. T., et al. "A Review on mechanical & microstructural property evaluation of Aluminum 5083 alloy weldment." *vol 3* (2013): 119-128.
23. Rao, K. Prasad, et al. “Improvement in Corrosion Resistance of Friction Stir Welded Aluminum Alloys with Micro Arc Oxidation Coatings.” *Scripta Materialia*, vol. 58, no. 11, Elsevier BV, June 2008, pp. 998–1001.
24. Jian Wang, Kai Zhu, Weichen Zhang, Xiaolei Zhu, Xiaofeng Lu, ‘Microstructural and defect evolution during WAAM resulting in mechanical property differences for ER5356 component’, *Journal of Materials Research and Technology*, Volume 22, 2023, Pages 982-996, ISSN 2238-7854.

25. Yuan, Tao, et al. "Loss of Elemental Mg During Wire + Arc Additive Manufacturing of Al-Mg Alloy and Its Effect on Mechanical Properties." *Journal of Manufacturing Processes*, vol. 49, Elsevier BV, Jan. 2020, pp. 456–62.
26. Tawfik, M. M., et al. "Effect of Travel Speed on the Properties of Al-Mg Aluminum Alloy Fabricated by Wire Arc Additive Manufacturing." *Journal of Materials Engineering and Performance*, vol. 30, no. 10, Springer Science+Business Media, June 2021, pp. 7762–69.
27. Su, Chuanchu, et al. "Effect of Heat Input on Microstructure and Mechanical Properties of Al-Mg Alloys Fabricated by WAAM." *Applied Surface Science*, vol. 486, Elsevier BV, Aug. 2019, pp. 431–40. Zuo, Wei, et al. "Effects of Solution Treatment Temperatures on Microstructure and Mechanical Properties of TIG–MIG Hybrid Arc Additive Manufactured ER5356 Aluminum Alloy." *Metals and Materials International*, vol. 24, no. 6, Springer Science+Business Media, Aug. 2018, pp. 1346–58.
28. Kim, Ho-Kyung. "Low-temperature Creep Behavior of Ultrafine-grained 5083 Al Alloy Processed by Equal-channel Angular Pressing." *Journal of Mechanical Science and Technology*, vol. 24, no. 10, Springer Science+Business Media, Oct. 2010, pp. 2075–81.
29. Hayes, R. W., et al. "A Preliminary Creep Study of a Bulk Nanocrystalline Al-Mg Alloy." *Scripta Materialia*, vol. 41, no. 7, Elsevier BV, Aug. 1999, pp. 743–48.
30. Xu, Xiaojing, et al. "Effect of Mn Content on Microstructure and Properties of 6000 Series Aluminum Alloy." *Applied Physics A*, vol. 125, no. 8, Springer Science+Business Media, July 2019.
31. Zhang, X., Guo, M., Zhang, J. et al. Dissolution of Precipitates During Solution Treatment of Al-Mg-Si- Cu Alloys. *Metall Mater Trans B* **47**, 608–620 (2016).
32. Singh, S., Jinoop, A. N., Kumar, G. T. a. T., Palani, I. A., Paul, C. P., & Prashanth, K. G. (2021).
33. Effect of interlayer delay on the microstructure and mechanical properties of

- wire arc additive manufactured wall structures. *Materials*, 14(15), 4187.
34. Kishore, V. S. N., & Vineesh, K. (2021). Temperature evolution in disc brakes during braking of the train using finite element analysis. *Materials Today: Proceedings*, 41, 1078–1081.
35. URL: [vehiclefreak.com/how-hot-does-a-combustion-chamber-get-in-a-vehicle](http://vehiclefreak.com/how-hot-does-a-combustion-chamber-get-in-a-vehicle)
36. Yanfei Geng, Irina Panchenko, Xizhang Chen, Yurii Ivanov, Sergey Konovalov, Wire arc additive manufacturing Al-5.0 Mg alloy: Microstructures and phase composition, *Materials Characterization*, Volume 187,20

